



---

# Global Warming through Wave Function Collapse

---

THESIS

submitted in partial fulfillment of the  
requirements for the degree of

BACHELOR OF SCIENCE

in

PHYSICS

Author : G.L. van de Stolpe  
Student ID : s1425781  
Supervisor : Prof. dr. ir. T.H. Oosterkamp  
2<sup>nd</sup> corrector : Dr. W. Löffler

Leiden, The Netherlands, May 25, 2019



# Global Warming through Wave Function Collapse

**G.L. van de Stolpe**

Huygens-Kamerlingh Onnes Laboratory, Leiden University  
P.O. Box 9500, 2300 RA Leiden, The Netherlands

May 25, 2019

## **Abstract**

We investigate thermal force noise on an ultracold cantilever



# Contents

<b>1</b>	<b>Introduction</b>	<b>1</b>
<b>2</b>	<b>Theory</b>	<b>3</b>
2.1	Continuous Spontaneous Collapse	3
2.1.1	Objective Collapse Theories	3
2.1.2	Introduction to Continuous Spontaneous Localization	4
2.1.3	CSL Parameters in Cantilever Setup	6
2.2	Cantilever dynamics	8
2.2.1	Force sensor transfer function	8
2.2.2	Thermally driven cantilever	9
2.2.3	Cantilever Driven by Excess Noise Source	10
2.3	Other Noise Sources	11
2.3.1	Noise Acting on the Cantilever	11
2.3.2	Noise Acting on the Measurement Device	12
<b>3</b>	<b>Methods</b>	<b>13</b>
3.1	Setup	13
3.1.1	Detection Mechanism	13
3.1.2	Thermalization	13
3.1.3	Cantilevers	14
3.1.4	Vibration Isolation and Filters	15
3.1.5	Signal Read-out and Storage	16
3.2	Measurements	16
3.2.1	Temperature Sweep	16
3.3	Data Analysis	16
3.3.1	Cantilever Simulation	16
3.3.2	Energy Measurement	17
3.3.3	File Merging	21

---

3.3.4	Q-factor	22
3.3.5	Position to Voltage Conversion	28
3.3.6	Computing the Excess Noise	30
<b>4</b>	<b>Results</b>	<b>31</b>
4.1	Measurement Overview	31
4.2	CSL Measurement Run 43 (17-12-2018)	32
4.2.1	Cantilever Energy	32
4.2.2	Excess Noise	32
4.2.3	Continuous Spontaneous Localization Bounds	36
4.2.4	Data Disclaimer	37
4.3	Mechanical Noise	39
4.3.1	Mechanical Disturbance	39
4.3.2	Improvements of the Mechanical Isolation	41
4.3.3	Pulse Tube Noise Reduction	44
4.4	Energetic Coupling to the Environment	46
4.4.1	Saturation Behaviour	46
4.4.2	Coupling to a Second Heat Bath	48
4.4.3	Coupling Mechanism	50
4.4.4	Modelling Saturation Behaviour	53
<b>5</b>	<b>Outlook</b>	<b>57</b>
5.0.1	Possible Improvement	57
5.0.2	Current Setup	57
5.0.3	Improved Setup	59
5.0.4	The Future of CSL	59
<b>6</b>	<b>Appendix</b>	<b>61</b>

# Introduction

Possibly the most challenging problem physics is facing today is the ongoing quest for the unification of the two major theories of the 20<sup>th</sup> century: Quantum Mechanics (QM) and General Relativity (GR) [1]. The general scientific consensus states that QM is the more fundamental theory and GR follows as a macroscopic approximation [2]. However, this transition from the microscopic to the macroscopic regime is poorly understood, as the Schrödinger equation and its accompanying wave function do not smoothly connect with the point particle description of Newtonian-Einsteinian mechanics [3]. The physical implication: while microscopic entities (e.g. single electrons) can live as a superposed wave function, macroscopic objects cannot. As soon as a microscopic object becomes entangled to its environment, for example by the act of measurement, it is forced out of superposition and can suddenly be described by a single set of definite coordinates. This phenomenon is known as the *measurement problem* [4].

In the popular Copenhagen interpretation the problem is qualitatively described under the name of *wave function collapse*. As soon as a measurement is done, Schrödinger's equations of motion are no longer valid and the wave function peaks at a well defined location, a stochastic process whose probability distribution is given by the square of the wave function. After the measurement the wave function evolves back to the spread out state, but in a fashion that guarantees that a second measurement immediately after the first yields exactly the same result [5]. There exists no mathematical framework for this behaviour and therefore Copenhagen devotees have to cope with this solely qualitative description [6].

Feasible alternatives called *objective collapse theories*, do provide a mathematically rigid framework. They pose that the wave function of a particle

is continually collapsing, be it at an extremely small rate (about once every  $10^{10}$  years [3]). However, when dealing with macroscopic objects (i.e. macroscopic number of particles) the particles' entanglement causes the object's entire wave function to be collapsing almost continuously. Ghirardi et al. [7] proposed a master equation to model this collapse, basically adding a stochastic collapse term to the Schrödinger equation, which leads to a small violation of conservation of energy. Further refinements of this concept now go under the name of *continuous spontaneous localization* (CSL) [8].

For experimental physicists, CSL provides an interesting research direction, as it is one of the few, if not the only, collapse theory that allows for rigorous testing and is falsifiable. Vinante et al. came up with a method to measure the violation of energy conservation as predicted by CSL, using a nanoscale force sensor [9]. The force sensor is a silicon cantilever in thermal equilibrium with a millikelvin temperature environment, where according to the equipartition theorem the thermal energy of the cantilever is equal to its kinetic energy. This kinetic term is measured by logging the movement of the tip and averaging over time, giving a value for the average temperature of the cantilever. If CSL is happening, it acts as a continuous source of heat, resulting in a cantilever that is always slightly warmer than its thermal bath. This extra heat can be measured and attributed to CSL.

The challenge of this kind of experiment is that it is generally very hard to be sure that the heating you are measuring is really CSL and not just some other noise source (e.g. thermal radiation, mechanical disturbance). Because of this, it has become customary to identify upper bounds to CSL heating instead of directly measuring its value. Naturally, for these bounds to be sufficiently low it is impervious to keep all noise sources acting on the cantilever to a minimum.

In this thesis we build upon the experiment as designed by Vinante et al. [10] focusing on the identification and analysis of several noise mechanisms that may influence the cantilevers energy. In chapter 2, an overview of the theoretical background of CSL and basic principles of atomic force microscopy is presented. Then, in chapter 3, we discuss our novel, flexible, way of data processing, which gives way to more accurate results. In chapter 4, both mechanical noise (section 4.3) and a thermal coupling to the environment (section 4.4) are investigated. The effects of improvements to the setup are reviewed and a model is proposed upon which further improvements may be based. Finally, we present a state of the art measurement from the current setup (4.2), which lowers CSL bounds by an order of magnitude.

# Theory

## 2.1 Continuous Spontaneous Collapse

### 2.1.1 Objective Collapse Theories

As explained in the introduction, the most popular interpretation of quantum mechanics, the Copenhagen interpretation, is built on two postulates[11].

1. A system evolves deterministically according to the linear Schrödinger equation before measurement.
2. The system undergoes non-deterministic projection when it interacts with a macroscopic system (measurement).

This interpretation is rather practical in the sense that it is based purely on heuristics. Indeed, one could argue that all the Copenhagen interpretation does is stating what is observed. Because no underlying principle is formulated, the interpretation becomes vague in its predictions when a system is examined that is in a regime where no heuristics have been acquired yet. Stated more concretely: what happens to system that is on the border between the microscopic and macroscopic, and where does this border lie?

Spontaneous collapse models offer a solution to this problem. They pose that the wavefunction is continually collapsing and that there is nothing special about the act of measurement. The only difference between microscopic and macroscopic systems is that macroscopic systems collapse at a much higher rate, attributed to many interacting particles who trigger each other's collapse. The formulation of such a model has to satisfy the following conditions [3]:

- Non-linearity: it should not be possible for macroscopic systems to be in a linear superposition
- Stochasticity: the measurements should be random and should obey the Born probability rule. Stochasticity is also needed to preserve causality, when non-linearity is introduced.
- Amplification: in microscopic systems, collapse should be practically unnoticeable, but in macroscopic many-particle systems the effect should be amplified so that the system will constantly be in the collapsed state.

### 2.1.2 Introduction to Continuous Spontaneous Localization

Continuous Spontaneous Localization (CSL) is currently the most popular model that satisfies the above conditions [9]. It makes clear, measurable predictions and is therefore the most interesting one to test experimentally. In order to develop an intuition for CSL, we describe its principles first qualitatively, before deriving measurable features quantitatively. This section is based on the extensive review of Bassi et al. [3].

CSL can be classified as a spatial collapse model, meaning that its collapse dynamics are designed to counter spatial superposition (contrary to energy collapse models) [3]. CSL counters these superpositions by stochastic collapses whose rate of occurrence is dependent on the system characteristics. In short, the less classical the state of a macroscopic system looks, the quicker it will collapse.

CSL is most intuitively understood in the framework of the density matrix formalism. The density matrix describes a quantum state as:

$$\hat{\rho} = \sum_{i,j} p_{ij} |\psi_i\rangle \langle \psi_j|. \quad (2.1)$$

The off-diagonal elements of the density matrix play an important role in the description of quantum states. They convey the information about the amount of superposition of the different basis states  $|\psi_i\rangle$ . When a system is classical, which means that  $|\psi_i\rangle$  cannot be in superposition, these off-diagonal terms are zero and the density matrix reduces to display the statistical distribution of the ensemble. Now, the aim for a collapse theory becomes clear: it has to entail a mechanism to make the off-diagonal terms shrink to zero quickly for large systems with significant superpositions.

To understand how CSL handles these dynamics, let us first look at the definition of the collapse rate  $\Gamma$  for a system of  $N$  nucleons:

$$\frac{\partial}{\partial t} \langle x''_i | \rho_t | x'_j \rangle = \Gamma(x'_i, x''_j) \langle x'_i | \rho_t | x''_j \rangle, \quad (2.2)$$

where  $|x'_i\rangle$  is the position basis state of particle  $i$  at position  $x = x'$ . Evidently, a system of one or more particles being in spatially separated superpositions of state  $|x'\rangle$  and  $|x''\rangle$  decays at a rate  $\Gamma$ . In more detail: in CSL the mass of particles is spread out over the position basis states and this spread evolves according to the decay rates. The expression for  $\Gamma$  contains two collapse triggers:

1. Single particle collapse
2. Multiparticle collapse

Single particle collapse is based on the demand that particles that are in a state where their mass is very non-localized should have a higher collapse rate. For a one particle system  $\Gamma$  is given by:

$$\Gamma(x', x'') = \frac{\gamma_{CSL}}{4\pi r_C^{3/2}} [1 - e^{-|x' - x''|^2 / 4r_C^2}], \quad (2.3)$$

where  $r_C$  is defined as the correlation length and  $\gamma_{CSL}$  is a universal physical constant. To clarify, equation 2.3 states the collapse rate of the state wherein the particle is in position  $x'$  and  $x''$  simultaneously. When we define  $l = |x' - x''|$ , it becomes clear that if  $l \ll r_C$  the decay rate goes to zero, but when  $l \approx r_C$  it grows approximately quadratically with  $l$ . Thus,  $r_C$  can be seen as nature's measure of toleration for long distance superpositions. This decay mechanism forces particles to have a Gaussian mass distribution of width  $r_C$ , as broader superposed states rapidly decay. To describe the typical timescale for which particles decay to their Gaussian form, the single particle collapse rate is defined:

$$\lambda_{CSL} = \frac{\gamma_{CSL}}{4\pi r_C^{3/2}}. \quad (2.4)$$

Multiparticle collapse is the mechanism that works as the collapse amplifier for dense systems. If two particles have a probability amplitude of being in the same location, or at least very near to each other:  $|x'_i - x'_j| \ll r_C$ , the total collapse rate of the system is further increased. Apparently, when one particle suffers from collapse, it forces collapse on

all other (superpositions of) particles that are in a vicinity  $r_C$ , hereby accelerating the collapse of the entire system. Intuitively, we can say that particle  $i$  actively decoheres particle  $j$ , which effectively shrinks the correlation length, which in turn drives particle collapse. This makes sense from the perspective that particles can be seen as mutually incoherent entities, almost from the definition that we consider them entities.

By further analysis, Adler et al. [12] showed that these effects of the two collapse drivers can be simplified into one equation for the decay rate of the whole system:

$$\Gamma = \lambda_{CSL} n^2 N, \quad (2.5)$$

where  $n$  is the number of particles within a cluster of range  $r_C$  and  $N$  denotes the number of these clusters. Naturally, the decay rate scales linearly with the number of particles in the system, as all single particle collapses add equally to the decay rate. The dependence on  $n^2$ , however, is caused by multiparticle collapse, i.e. single particles inducing collapse of neighbours. Every time particle  $i$  collapses its  $n$  neighbours also collapse, and the same holds the other way around: every time one of the neighbours collapses particle  $i$  also collapses. Thus, amplification scales with the number of unidirectional links in a complete graph of  $n$  particles:

$$L = n(n - 1) \approx n^2, \quad \text{for } n \gg 1. \quad (2.6)$$

Equation 2.5 is a handy rule of thumb which displays the two important drivers in CSL; the intricate cooperation between single- and multiparticle collapse, which results in a theory that is able to describe both microscopic superposition and macroscopic collapse using a consistent mathematical framework.

### 2.1.3 CSL Parameters in Cantilever Setup

#### CSL to Force Noise

Now that it has become clear how CSL counters the existence of macroscopic quantum states, the implications for the Hamiltonian of the cantilever setup are examined. The collapse behaviour described above can be mimicked by adding a stochastic potential to the Hamiltonian of the system:

$$V(t) = -\hbar w_t \sqrt{\eta} \hat{q}, \quad (2.7)$$

where  $\hbar$  is Planck's constant divided by  $2\pi$ ,  $w_t$  is white noise with zero average and delta correlation function,  $\hat{q}$  is the position operator and  $\eta$

holds information about the systems expected decay rate, similar to equation 2.5. In the cantilever system, following Vinante et al. [9], this term can be computed to be:

$$\eta = \frac{(4\pi)^{3/2} \lambda_{CSL} r_C^3}{m_0^2} \int \frac{d^3k}{(2\pi)^3} k_z^2 e^{i\mathbf{k} \cdot \mathbf{r}_C} |\tilde{\rho}(\mathbf{k})|^2. \quad (2.8)$$

Then, writing the contribution in terms of the Heisenberg equations of motion:

$$\partial_t \hat{q} = \frac{\hat{p}}{m}, \quad (2.9)$$

$$\partial_t \hat{p} = \hbar \omega_t \sqrt{\eta}, \quad (2.10)$$

the second being the quantum mechanical variant of a force. Because this force is stochastic, it increases quantum decoherence, driving decay of the off-diagonal terms of the density matrix as qualitatively described in section 2.1.2. For further analysis on the effect of this stochastic force on the movement of the cantilever it makes sense to express the term in the frequency domain, as cantilever dynamics can more easily be expressed this way. The excess force noise that the cantilever experience from collapsing of the wave function in the CSL model is then:

$$S_{F_{excess}} = 2\hbar^2 \eta \quad (2.11)$$

where the force is squared to arrive at a noise power spectrum, as is customary for noise sources.

### Force Noise in Cantilever Setup

Now that we understand how CSL leads to an excess force noise, we want to know what a measured force noise in our setup tells us about the parameters in the CSL model. We are interested in finding upper bounds for  $\lambda_{CSL}$  at different values for  $r_C$ . We approximate that for our setup, only the sphere contributes to CSL noise, as our cantilever has very low mass with respect to the sphere. Any extra CSL noise from the cantilever that we do not take into account would only increase the total force noise caused by CSL, further lowering our estimated upper bounds for  $\lambda_{CSL}$ . Then, we use the following formula from Vinante et al. [9]:

$$\lambda_{CSL} = \eta_s \left( \frac{(4\pi)^2 r_C^2 \rho_s^2}{3m_0^2} \left( 1 - \frac{2r_C^2}{R^2} + e^{\frac{R^2}{r_C^2}} \left( 1 + \frac{2r_C^2}{R^2} \right) \right) \right)^{-1}, \quad (2.12)$$

where  $R$  is the radius of the sphere,  $\eta_s \approx \eta = S_{F_{excess}} / (2\hbar^2)$ . Now, it is possible to estimate  $\lambda_{CSL}$  from an excess force noise, measured in experiment.

## 2.2 Cantilever dynamics

### 2.2.1 Force sensor transfer function

The cantilever acts as a force sensor in the way that its movement is wholly determined by an input force acting on it. In our experiment we constantly measure the displacement (position) of the cantilever (sometimes called the signal), so if we want to compute the (thermal) force noise that acts on the force sensor, we have to understand how this force noise is transferred into cantilever movement. For this we analytically determine the transfer function in the frequency domain, which is defined as:

$$H(\omega) = \frac{X(\omega)}{F_{ext}(\omega)}. \quad (2.13)$$

This transfer function is determined by the equations of motion for a damped resonator:

$$m \frac{\partial^2 x}{\partial t^2} = -kx - c \frac{\partial x}{\partial t} + F_{ext}, \quad (2.14)$$

where  $k$  is the spring constant,  $m$  the mass of the resonator and  $\gamma = \frac{c}{2m}$  is the damping factor [13]. Rewriting this in the frequency domain yields:

$$H(\omega) = \frac{1}{k - m\omega^2 + i\omega c}. \quad (2.15)$$

When we want to describe the cantilevers movement when it is driven by a noise source, we simply multiply the square transfer function with the force noise to get the position noise. We work with amplitude squares here because no phase information is known (inherent to noise),

$$S_x(\omega) = |H(\omega)|^2 S_F(\omega), \quad (2.16)$$

$$|H(\omega)|^2 = \frac{1}{(k - m\omega^2)^2 + c^2\omega^2}, \quad (2.17)$$

where  $S_F$  (in  $N^2 Hz^{-1}$ ) is the input force noise and  $S_x$  (in  $m^2 Hz^{-1}$ ) is the resulting position noise. If we integrate the position noise  $S_x(\omega)$  over the whole frequency domain we obtain an expression for the average cantilever displacement:

$$\langle \frac{1}{2} k x^2 \rangle = \frac{1}{2} k \int_{-\infty}^{\infty} x(t)^2 dt = \frac{1}{2} \frac{k}{2\pi} \int_0^{\infty} S_x(\omega) d\omega, \quad (2.18)$$

where we used Plancherel's theorem and the ergodic hypothesis following de Voogd et al. [14]. Typically, we measure the square of the displacement

and average over time, which scales as the energy of the cantilever. Now, we have arrived at the expression for this cantilever energy in terms of the input force noise:

$$\langle E_{cantilever} \rangle = \frac{1}{2} \frac{k}{2\pi} \int_0^\infty |H(\omega)|^2 S_F(\omega) d\omega. \quad (2.19)$$

## 2.2.2 Thermally driven cantilever

First, we examine the expected cantilever behaviour when it is solely thermally driven. In this scenario, the cantilever is coupled (in thermal equilibrium) to a heat bath with temperature  $T$ , which results in thermal motion. In order to predict the cantilever energy (eq. 2.19) when it is coupled to a thermal bath in this way, it is necessary to describe these effects in terms of the thermal force noise acting on the cantilever. This expression can be derived in an equivalent way to electrical Johnson noise and has the form [15][14]:

$$S_{F_{Thermal}} = \frac{4k_B T}{\omega} \text{Im} \left( \frac{F(\omega)}{X(\omega)} \right) = 4k_B T c = 8k_B T m \gamma \quad (2.20)$$

Note that  $S_{F_{Thermal}}$  is proportional to  $c$  and hence, the damping factor  $\gamma$ , which has a role analogous to the resistance  $R$  for the Johnson noise in an electrical circuit. To understand why the thermal force noise is proportional to the damping factor, we show that  $\gamma$  can also be interpreted as a measure of coupling to the thermal bath. To see this, we begin with the definition of the quality factor (Q-factor) of a resonator, which describes the cantilever's capacity to store energy in its motion:

$$Q = 2\pi \frac{E_{stored}}{E_{lost/cycle}} \approx \frac{\omega_0}{2\gamma'}, \quad (2.21)$$

where the approximation holds for large  $Q$ . This definition is used to formulate energy transfer between the cantilever and the heat bath:

$$P_{transfer} = E_{lost/cycle} \frac{\omega_0}{2\pi} = E_{stored} * 2\gamma. \quad (2.22)$$

Apparently,  $\gamma$  provides a measure for the energy coupling between the resonator and the heat bath. This coupling, and thus the expected thermal motion of the cantilever, is strongly dependent on the characteristics of the cantilever. As  $\gamma$  is inversely proportional to  $Q$ , high quality resonators, like our cantilever, are weakly coupled to the thermal bath and the expected force noise at a certain bath temperature will thus be lower.

Using the expression for the thermal force noise in equation 2.20 and equation 2.16, the position noise in thermal equilibrium is given by:

$$S_x(\omega) = \frac{4k_B T}{m} \frac{\frac{\omega_0}{Q}}{(\omega_0^2 - \omega^2)^2 + (\frac{\omega_0 \omega}{Q})^2}, \quad (2.23)$$

where we have substituted in the Q-factor. For high values of Q (under-damped systems) equation 2.23 can be approximated by a Lorentzian [14]:

$$S_x(\omega) \approx \frac{k_B T}{k} \frac{\frac{\omega_0}{Q}}{(\omega_0 - \omega)^2 + (\frac{\omega_0}{2Q})^2}, \quad (2.24)$$

Taking the integral over frequency space of this spectrum as in equation 2.18, shows that the cantilever obeys the equipartition theorem:

$$\langle \frac{1}{2} k x^2 \rangle = \frac{1}{2} \frac{k}{2\pi} \int_0^\infty S_x(\omega) d\omega = \frac{1}{2} k_B T, \quad (2.25)$$

Note that this integral is always conserved in thermal equilibrium, independent on the specific shape of the Lorentzian. In as much as that the location of the peak (at the resonance frequency  $\omega_0$ ) and the width of the peak (determined by the Q-factor) only influence where and how local the cantilever energy is distributed in the frequency domain, not the total energy of the signal ( $\frac{1}{2} k_B T$ ).

### 2.2.3 Cantilever Driven by Excess Noise Source

Next, we want to add a non-thermal white force noise as we expect from CSL (defined in equation 2.11) and see how that affects the cantilever energy from equation 2.19. The main conceptual difference of this excess source with respect to a thermal source is that its magnitude does not depend on the Q-factor, as it is not in equilibrium with the cantilever. A pure white noise source violates the local conservation of energy that is present in thermal equilibrium with a heat bath. Combining both sources, the input force noise becomes:

$$S_F = S_{F_{Thermal}} + S_{F_{Excess}} \quad (2.26)$$

And the cantilever energy is given by:

$$\langle E_{cantilever} \rangle = \frac{1}{2} \frac{k}{2\pi} \int_0^\infty |H(\omega)|^2 (S_{F_{Thermal}} + S_{F_{Excess}}) d\omega \quad (2.27)$$

As both sources do not depend on the frequency, the terms can be pulled out of the integral. Next, the integral over the transfer function squared can easily be seen from equation 2.25:

$$\int_0^\infty |H(\omega)|^2 d\omega = \frac{\pi}{4km\gamma} \quad (2.28)$$

Leading to the following formula for the cantilever energy:

$$\langle E_{cantilever} \rangle = \frac{1}{2}k_B T + \frac{1}{16m\gamma} S_{F_{Excess}} \quad (2.29)$$

Since the objective of the experiment is to estimate the (constant) excess force noise, the  $\gamma$  as a prefactor is impractical as it might be subject to change with respect to temperature. Hence, the left and right side of equation 2.29 are divided by  $Q$  to arrive at the following relation:

$$\frac{\langle E_{cantilever} \rangle}{Q} = \frac{1}{2}k_B \frac{T}{Q} + \frac{1}{8m\omega_0} S_{F_{Excess}} \quad (2.30)$$

When measurements of the cantilever energy and the Q-factor are done, the left side of equation 2.30 can be plotted as a function of  $\frac{T}{Q}$ , resulting in a linear relation with slope  $\frac{1}{2}k_B$  and offset  $(8m\omega_0)^{-1} S_{F_{Excess}}$ .

## 2.3 Other Noise Sources

### 2.3.1 Noise Acting on the Cantilever

#### Mechanical Excitation

In the previous section, the cantilever is expected to be driven solely thermally. However, mechanical vibrations originating from outside (or inside) the cryostat might also excite the cantilever. These mechanical "bumps" will result in a temporary higher cantilever energy than expected from a solely thermally driven cantilever. After such an excitation the cantilever will decay back to its expected energy by dissipating its "excess heat" to the coupled thermal bath. However, for the measurements of the cantilever energy long averages are taken, leading to a systematic overestimation of the thermal energy, as mechanical spikes in the energy are also taken into account in the average. Considerable effort was made to reduce this noise source, as is described in section 3.1.4 and section 4.3, but completely eliminating mechanical noise remains a challenge today.

### Thermal radiation

Another source of noise could be some electrical component close to the cantilever radiating warmth on it, hereby raising its temperature with respect to the heat bath. This extra source of heating would be very hard to identify, as it is typically a white noise source. However, thermal radiation is known to fall off as  $T^{-4}$  and hence we expect little contribution from this noise at milliKelvin temperatures. Also, much of the setup around the cantilever is gold plated to counter blackbody radiation from the copper underneath. We use the Stefan-Boltzmann law to calculate the expected power on the cantilever when its environment is  $100mK$  (ten times warmer than the cantilever itself). This results in a radiated power of  $100yW$ , negligible with respect to other noise.

### Upper bounds

Because of the possibility that mechanical vibration, thermal radiation and maybe other white noise sources still act on the cantilever a force noise measurement can only be used to identify an upper bound for the CSL contribution to the cantilever movement. It is inherent to these kind of measurements that it is very hard to prove that the measured noise is actually CSL, as it is virtually impossible to rule out every other possible noise source.

### 2.3.2 Noise Acting on the Measurement Device

Noise that is present in the measurement device (SQUID) or in the connecting cables will reduce the accuracy with which we can measure the cantilever position at a certain point in time. However, it will not influence the energy measurement as large averages over the cantilever energy are taken for this. Also, this source of noise does not contribute significantly to the error on the determination of the Q-factor, as is explained in section 3.3.4.

## Methods

### 3.1 Setup

#### 3.1.1 Detection Mechanism

The force sensor that is used for detecting the force noise is a nanomechanical resonator, called the cantilever, which is placed inside a dilution refrigerator, where its temperature can be minutely controlled. Its movement is detected according to previous work by Usenko et al. [16]. Here, a short overview is given.

A magnetic bead (diameter  $1 - 10\mu\text{m}$ ) attached on the tip of the cantilever provides a means to detect the movement. This is done by placing a pick-up loop underneath the cantilever, laid on a silicon detection chip. On this chip, a piece of copper called the *sample* and an RF wire are located as well, which are used for magnetic resonance force microscopy (MRFM) measurements. A drawing of the setup can be seen in figure 3.1.

As the cantilever moves, the flux through the loop varies. This flux change is then transferred to an alternate circuit that is in the vicinity of a dc Superconducting Quantum Interference Device (SQUID). This device can very accurately measure and amplify the flux that falls on its detector (up to a multitude of  $\Phi_0$ ) and converts it into a voltage. With the use of a flux-locked loop, the output voltage of the SQUID scales linearly with the input flux, and thus the cantilever movement.

#### 3.1.2 Thermalization

The cantilever is thermally anchored to the bottom (third) mass of a vibration isolation mass spring system, which we call "mass 3". This mass

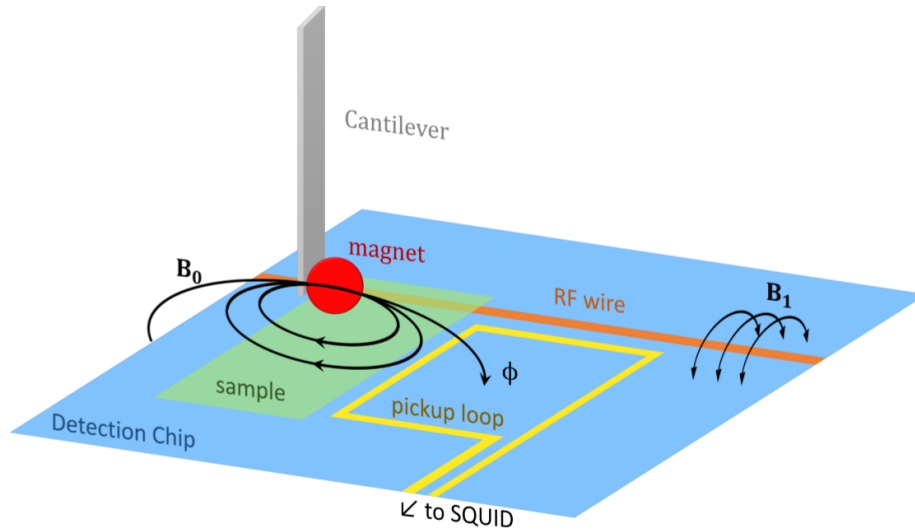


**Figure 3.1: Schematic drawing of the setup.** The magnetic bead on the cantilever leads to a flux through the pick-up loop, located on a silicon detection chip. The sample and RF wire are used for MRFM and are not relevant for our experiment. This image was taken from the dissertation of de Wit [17]

can be set to a specific temperature (above the temperature of the mixing chamber) with a local heater and thermometer, using a feedback loop in the LabView Virtual Instrumentation "20170807 - PID Yeti.vi". This allows us to set the cantilever temperature remotely. Furthermore, the cantilever chip rests in a metal holder, containing a piezoelectric element which can be used to drive the cantilever mechanically.

### 3.1.3 Cantilevers

The cantilever that was used in our experiments, which we call the "ladder cantilever" was produced by the Degen group at ETH Zurich. The ladder structure of this sensor potentially gives it a very high Q-factor, of the order of  $4.5 \times 10^4$  at 140 mK [18]. Its spring constant was measured to be  $k = 19.6 \mu\text{Nm}^{-1}$  in Zurich before the magnetic bead was attached. The magnetic bead has a radius of  $R = 1.21 \mu\text{m}$ , measured in a SEM. The diameter of the bead suggests a mass of  $m = 5.51 \times 10^{-14}$  kg, leading to an expected resonance frequency of 3.00 kHz. However, when the cantilever was cooled to cryogenic temperatures, the resonance frequency was measured to be 5395 Hz. Because the mass had not changed, it was posed

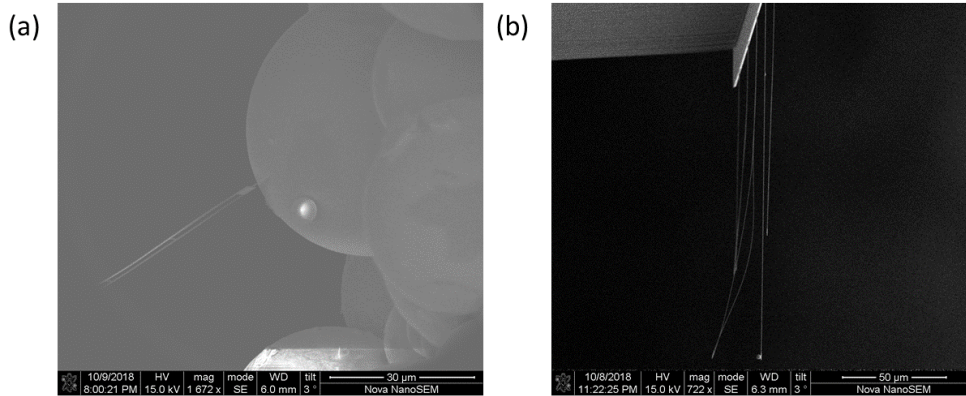


**Figure 3.2:** SEM image of the ladder cantilever that was used in the experiments. a) Close up where the ladder structure is visible. b) Overview where the magnetic bead can clearly be seen, attached to the tip of the cantilever.

that the spring constant was altered, possible due to the low temperature environment or through applied mechanical strain during the attachment of the magnetic bead. This adjusted spring constant was calculated to be  $k = 63.4 \mu\text{Nm}^{-1}$ . Also, the resonance frequency became dependent on the distance from the pick-up loop and the temperature of the copper sample underneath, as will be explained in more detail in section 4.4. Scanning electron microscope images of the ladder cantilever can be seen in figure 3.2.

### 3.1.4 Vibration Isolation and Filters

As was mentioned above, the cantilever is secured on the bottom mass of a mass spring system, which is put in place to reduce mechanical vibrations from outside the cryostat exciting the cantilever. Details on the mass spring system and its performance can be found in reference [19].

The SQUID voltage that is induced by the cantilever is carried by NbTi coaxial cables to a so called break-out box, through which the signal is transferred to room temperature. An **attenuator** is present on the cantilever chip to stop Johnson noise from exciting the piezoelectric element.

### 3.1.5 Signal Read-out and Storage

From the break-out box, the SQUID voltage is connected to a Stanford Research Systems voltage preamplifier, where the signal is amplified (typically 10 times) and a high pass filter (0.03 Hz) is applied to dispose of a DC voltage offset. Then, it is led into a DAQ-card which digitalizes the signal, and fed into the USB port of a PC. The LabView VI "write\_TDMS.vi" reads in the signal and stores 10 minute long files, with a sampling frequency of 50kHz. The files are labeled automatically with the date and time upon which they were created as "TDMS\_yyyymmdd\_hhmmss.tdms". The files are stored in folders along with the temperature data of the data set.

## 3.2 Measurements

### 3.2.1 Temperature Sweep

The most logical way to measure the excess noise in our system is by sweeping the temperature of the cantilever as is done in reference [10] and [10]. A script is written in LabView to automatically change the set temperature of mass 3 using "20170807 - PID Yeti.vi". This set temperature is held constant with a heater on mass 3, using feedback. The temperature data and signal are stored continuously, the latter in 10 minute files as described in section 3.1.5.

## 3.3 Data Analysis

### 3.3.1 Cantilever Simulation

In order to develop an intuition for the behaviour of the cantilever and to evaluate the accuracy of quantitative analysis methods, it makes sense to write a simulation of the cantilever signal when it is driven by white noise (thermal or excess). In this simulation the cantilever signal is mimicked using the Fourier space transfer function. First, the specifications of the cantilever, parameters for data acquisition (e.g. sampling frequency  $F_s$ ) and parameters for data analysis are set. Then, the cantilever signal is simulated, using the following operations:

- A white noise signal is generated by a random number generator. This noise has a cutoff frequency that is half the sampling frequency  $F_s$  that is used.

- The Fast Fourier Transform (FFT) of the white noise is taken to obtain its Fourier transform.
- The FFT is multiplied by the transfer function from equation 2.15 with input specifications, to get the cantilever signal in the frequency domain.
- An inverse FFT is done on this product, to get the cantilever signal in the time domain.
- Extra noise is added to the cantilever signal, mimicking noise induced by the measurement apparatus, by adding another white noise source. This source is generated by random number generator, with cutoff  $F_s$  and amplitude that is dependent on the desired SNR.

The characteristics of the simulated cantilever were chosen to be  $k = 1e6\text{Nm}$ ,  $m = 1\text{kg}$ ,  $Q = 1000$ , resulting in a resonance frequency of  $f_0 = 159\text{Hz}$ . These specifications are different from the actual cantilever, but they ease the load of computation, as a lower sampling rate is needed at this resonance frequency. The sampling rate was chosen to be  $F_s = 500\text{Hz} > 2f_0$ , so that the Nyquist theorem is satisfied. Although the Q-factor is much lower than that of the ladder cantilever, the correlation time is comparable because of the lower resonance frequency and thus the Q-factor measurement is actually very similar.

### 3.3.2 Energy Measurement

#### Digital Lock-in Amplifier

To measure the energy of the cantilever as described in equation 2.30, the equipartition theorem as described in equation 2.25 is used. This is done by measuring the average of the square of the amplitude of the cantilever signal. Certainly, it is not desirable to average the whole signal in the time domain, as this contains all sorts of frequency dependent noise, easily drowning out the cantilever signal and thus leading to an SNR much smaller than one. Also, the thermal contribution is dependent on bandwidth. To do away with this problem we only measure the amplitude at and directly around the cantilever resonance frequency, using a digital lock-in amplifier. It can be justified to throw away all the signal at lower and higher frequencies, as the high Q-factor of the cantilever assures that the bulk of the thermal noise signal is very localized around the resonance frequency.

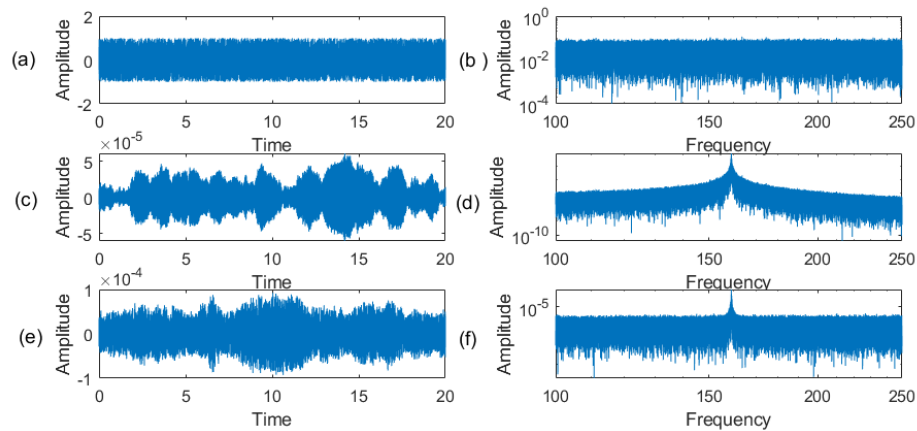


**Figure 3.3: Simulation of the cantilever signal.** Intermediate steps for the simulation of the cantilever signal, showing the time domain signal to the left, and the frequency domain to the right. In (a) the input white noise can be seen, (b) shows the accompanying spectrum, (c) the cantilever signal, (d) the cantilevers spectrum, (e) the cantilever signal with added noise and (f) the spectrum of this signal with added noise. Used cantilever specifications were:  $k = 1e6$ ,  $m = 1$ ,  $Q = 1000$ . The sampling rate was chosen to be  $F_s = 500 > 2f_0$ .

A digital lock-in amplifier is a digital post processing method designed to mimic the behaviour of an analog lock-in. The great advantage is that the raw data of the signal is stored on the computer, so that one can still adjust the lock-in settings for a dataset after the measurement is done. The digital lock-in works in a similar way as its analogous counterpart and can best be visualized in the frequency domain. First, a fit is done on the spectrum of every 10 minute file to find the exact resonance frequency of the cantilever for that piece of data (this frequency can be temperature or position dependent). The lock-in frequency is chosen to be equal to this resonance frequency. Then, the raw cantilever signal is multiplied by a sine function at the lock-in frequency and is therefore convoluted with a delta peak in frequency space at this frequency. Through this convolution the signal is shifted so that the amplitude at the lock-in frequency now lies at zero frequency. Then, a low pass filter (butterworth, second order) is applied to filter out the remaining noise, which now lies at higher frequencies. The procedure is repeated, using a cosine at the lock-in frequency instead of a sine to get the out-of-phase component. The combination of the two reveals the amplitude of the raw signal within a certain bandwidth around the lock-in frequency, which is determined by the cutoff frequency of the applied low pass filter. The energy of the signal, which scales as

$V^2 \propto x^2$ , can then be found by taking the square of the in-phase and out-of-phase components and summing them. As the raw signal is typically sampled at a very high rate (e.g. 50kHz), after this step a data reduction is done, reducing the time resolution to 100Hz. To achieve this, the signal is averaged over 10 ms steps. Note that the data reduction has no implications for the resolution of the signal at this point, as its time resolution is already limited by the cut off frequency of the applied low pass filter, which is typically order 10Hz.

### Noise Reduction

It still remains unclear how the cut off frequency of the low pass filter should be chosen. Typically, lock-in amplifiers introduce a trade-off to the measurement. If one wants to decrease the bandwidth around the desired frequency, a lower cutoff for the filter is chosen. However, this has the direct implication that the time resolution is limited to the cutoff frequency and no higher frequency fluctuations of the signal can be observed. In our experiment, we actually want to measure at frequencies around resonance, because the Lorentzian has a certain width and it is undesirable to throw away a part of the cantilever energy.

One way to choose the cutoff frequency is by demanding the signal has the highest SNR, where the SNR over a certain bandwidth is defined as follows:

$$SNR = \int \frac{Signal}{S_{app}} df, \quad (3.1)$$

where  $S_{app}$  is the noise of the measurement apparatus, which can be determined experimentally. Also, the SNR at resonance can be defined as:

$$SNR_{res} = \frac{Peak\ Height}{S_{app}} \quad (3.2)$$

Maximization of equation 3.1 leads to the condition:

$$S_{app} = |H(2\pi f_c)|^2, \quad (3.3)$$

where  $f_c$  is the cutoff frequency and  $H(\omega)$  is the transfer function from equation 2.17. Choosing a cutoff frequency larger than  $f_c$  would add more noise than cantilever signal and would therefore lower the SNR. However, if the noise floor is very high compared to the cantilever signal, a large percentage of the cantilever energy will be thrown away, possibly leading to distorted image of the cantilever energy. The reason for this is that the energy at the peak scales with the Q-factor, while the total energy in the

Lorentzian does not. Hence measuring at a very small bandwidth around the resonance frequency (order 0.01Hz) will add a Q-factor dependence. Another, more robust, way to set the condition for the cutoff frequency is to formulate it in an integral form: the signal that is missed should not be bigger than the total noise that has been added so far. In mathematical terms:

$$\int_{f_0}^{f_0+f_c} S_{app} df = S_{app} f_c = \int_{f_0+f_c}^{\infty} |H(2\pi f)|^2 df. \quad (3.4)$$

This formulation guarantees that even when the noise is relatively high, a big part of the signal is taken into account.

Because we use a digital lock-in, no a priori choice is made with respect to the optimal cutoff frequency and this freedom remains with us until data analysis. Also, because the whole signal, and thus the whole spectrum, is recorded, one has the freedom to exploit all this information in the data processing. Therefore, an even better choice for the cutoff frequency is to make sure at least a certain part of the cantilever energy is captured (e.g. 99%). The apparent drawback that a lot of noise is also taken into the signal can be countered in the following way: because we have access to the whole spectrum we can set another digital lock-in at a frequency some  $\Delta f$  away where the cantilever has practically decayed and we measure just the noise background. We then subtract this background energy from the signal energy, in this way becoming independent on the magnitude of the noise floor. This method is improved upon by setting a noise lock-in both to the left and to the right of the resonance frequency and taking an average before subtracting.

To evaluate the performance of these methods; choosing a smart cut-off or subtracting the background, the energy of the cantilever signal is computed for different lock-in bandwidths. It can be seen that when the cut off frequency is chosen to be more than three times the peak width, background reduction becomes important as the noise becomes significant with respect to the cantilever signal.

Evidently from figure ??, the background reduction method best satisfies our demand for an accurate energy measurement. As can be seen in figure 3.5, using this technique, the measured energy becomes completely independent of the SNR. To determine a reasonable standard cutoff frequency, we examine a real measured cantilever signal and inspect how the energy increases with the cutoff frequency. It is found that for the cantilever specifications in the experiment, more than 99% of the energy is taken into account when the cutoff frequency is set to 5Hz, which is about 10 times the FWHM of the peak. Therefore, 5 Hz is chosen to be the stan-

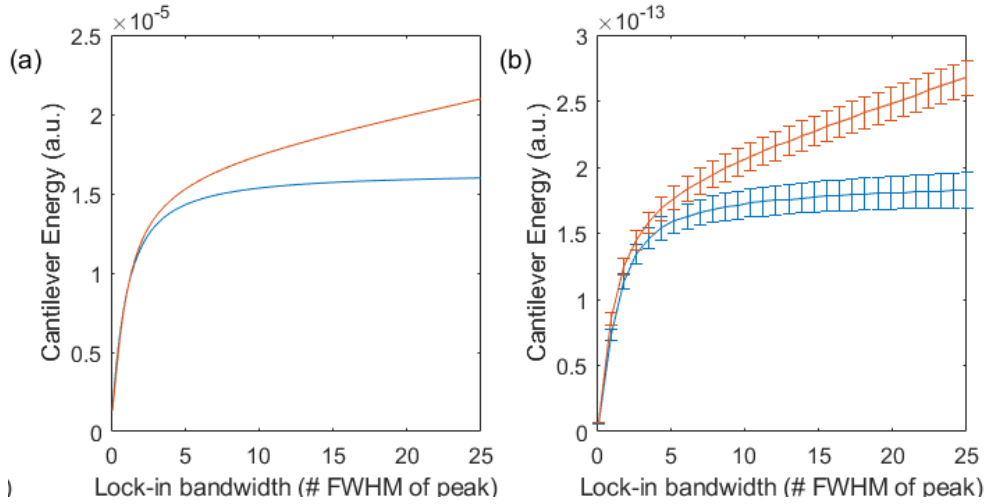


**Figure 3.4:** Measured energy as function of the lock-in bandwidth without background reduction (red) and with background reduction (blue) for simulated (left) and experimental data (right). The simulated signal has an  $SNR_{res} = 986$ . The experimental data is from a 10 minute cantilever measurement (filename: TDMS\_20181227\_232358.tdms).

dard cutoff frequency when using background reduction.

### 3.3.3 File Merging

As described in section 3.1.5, the cantilever signal is stored in 10 minute files. To be able to do longer measurements than this, individual files are merged after the digital lock-in is applied. At the beginning of each file, spikes in the cantilever signal were seen, presumably due to the SRS amplifier resetting its filters (as these are set by the LabView Virtual Instrument write\_TDMS.vi every time a new file is created). To do away with these false signals, the first two seconds of every ten minute file were deleted.

Because time measurement accuracy can be important for the mechanical measurements, a code was written to ensure synchronization between the temperature file and cantilever signal.

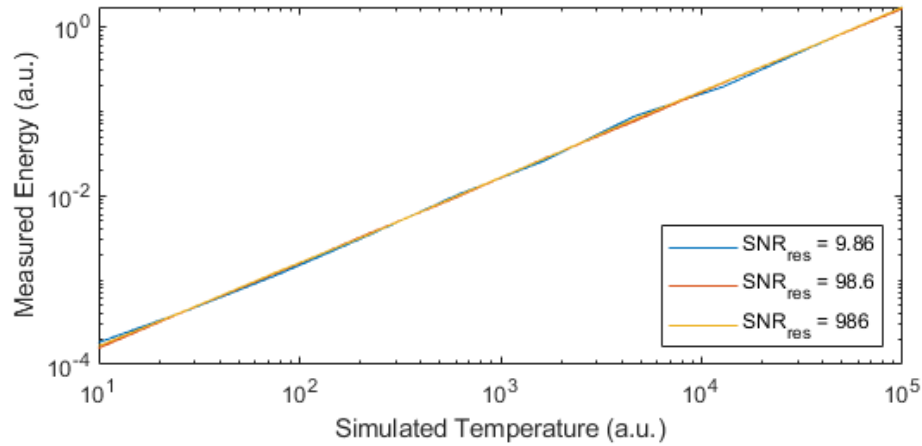


**Figure 3.5: Energy measurement dependence on SNR, using background reduction.** When background reduction is employed, an decreasing SNR has no visible effect on the measured energy over a wide range. The input white noise scales linearly with the simulation temperature. The simulated files were 5000 correlation times long (independent measurements, explained in section 3.3.4), and cantilever specifications were the same as in figure 3.3.

### 3.3.4 Q-factor

#### Measurement Principle

When looking at equation 2.30, it is obviously important to be able to measure the Q-factor accurately. Especially because  $Q$  typically changes with temperature. If these changes are not corrected for, the expected linear relation will be affected, showing positive or negative deviations with lower or higher Q-factor, respectively. Ideally, measuring the Q-factor should be done during the data acquisition for the energy measurement, to minimize the risk of unnoticed changes. The most conventional way of measuring the Q-factor of a resonator is by examining its signal in the frequency domain. This is done by either driving the cantilever at different specific frequencies (sweep) or by averaging the signal when it is driven by white noise and taking a spectrum. Both methods map out the specific shape of the Lorentzian function 2.24. By numerical fitting, the quality factor can be extracted.

For our purposes, driving the cantilever is not a good option, as we do not want to heat up the cantilever during or in between measurements. A way around this would be to do detailed measurements on the dependence of  $Q$  beforehand. However, because the quality factor is highly tem-

perature dependent, driving it at different magnitudes already alters  $Q$ ].

By taking long averages and taking the spectrum, we can obtain data similar to sweep data. Two important obstacles remain: first, the cost function for fitting the Lorentzian function is ill-defined. Fit weights can be tuned in order to ensure that either the tails or the peak are given priority and this is often done on intuition. Second, and more importantly, when there is a drift in the resonance frequency during the average time, we observe frequency jitter. This will lead to a broader peak, resulting in a lower estimation of the  $Q$ -factor.

Another, more robust, way of measuring the  $Q$ -factor is through the autocorrelation function. It has the great advantage that the analysis is done in the time domain, thereby rendering it immune to frequency related defects. The method can be made intuitive by looking at equation 2.22. As a higher  $Q$  means that cantilever energy is lost (or gained) at a slower rate, we expect subsequent cantilever energy measurements to be more correlated with high  $Q$ . We can compute this difference using the autocorrelation function:

$$R_{EE}(t_2) = \langle (E(t_1) - \bar{E})(E(t_1 + t_2) - \bar{E}) \rangle \quad (3.5)$$

Where  $E(t)$  is the cantilever energy and  $\bar{E}$  is the average cantilever energy. The second is subtracted in order to correct for the fact that the energy  $E \propto x^2$ , in contrast to the position  $x$ , is always positive. If we were to neglect this correction, uncorrelated signals in  $x$  would still have a non-zero correlation in  $E$ , because there is no negative component to cancel out the positive contribution.

From the autocorrelation function we observe an exponential decay, characterized by correlation time  $\tau$ . From this parameter, the  $Q$ -factor can be easily computed:

$$R_{EE}(t_2) \propto e^{-\frac{2t_2}{\tau}}, \quad (3.6)$$

$$Q = \frac{\omega_0 \tau}{2}, \quad (3.7)$$

where  $\tau$  is the correlation time. The factor 2 arises from the fact that the correlation time is defined for the position of the cantilever in stead of the energy.

## Computation

A function was written to compute the  $Q$ -factor from a cantilever energy dataset, which is made with the digital lock-in as described in section 3.3.2.

Matlabs `xcorr()` function computes the autocorrelation function from equation 3.5, with a max lag time of 50 seconds. Then, `lsqcurvefit()` is used to fit the function  $P_1 e^{P_2 x}$ ,  $P_1$  and  $P_2$  being the fit parameters. The fit is done over only a part of the data to get an optimal result. The first  $\frac{1}{f_c}$  seconds are not used for fitting as the low pass filter of the lock-in (whose cut off is  $f_c$ ) induce an extra auto correlation in this regime. A maximum fitting time is also employed, as the fit error is dependent on the range of the fit. The parameter  $P_2$  is then used to find the Q-factor according to equations 3.6 and 3.7.

### Error Estimation

It is important to have a reliable estimation of the error on the Q-factor as the uncertainty on the measured excess noise depends on it. The error in Q-factor estimation is expected to fall off as  $\frac{1}{\sqrt{N}}$ , where  $N$  is the number of correlation times that fit into the length of the cantilever energy file, as the correlation function is averaging over all these independent samples. We expose this relationship by simulating multiple cantilever energy files with known Q-factor. Next, we compute the Q-factor for different lengths of these energy files and determine the relative error with respect to the input Q-factor. Also, some error will arise because of the fitting procedure.

First, we optimize the fitting procedure by changing the fitting range of the data. When varying the length of the fitting from  $\frac{\tau}{4}$  to  $2\tau$ , it is seen in figure 3.6 that smaller fitting ranges lead to better results. This can be understood from the fact that noise on the measured auto correlation function has less destructive impact when the amplitude is large (when  $t < \tau$ ). From figure 3.6 that the fit time is best when the maximum of the fit range is set to  $\frac{\tau}{4}$ . However, when we examine the fit by eye, it seems to describe the correlation function very good in the whole range  $[\frac{\tau}{4}, \tau]$ . In actual cantilever experiments, the fit time is set to three seconds, which is approximately one correlation time.

To delve deeper into the estimation of the error in Q-factor we examine the standard deviation over a larger number of simulations. The mean relative error and associated standard deviation are plotted in figure 3.7. We choose our estimation of the error to be:

$$\epsilon = (\epsilon_0 \pm \sigma_0) \frac{1}{\sqrt{N}} \quad (3.8)$$

where the prefactor  $\epsilon_0 = 1.48$  and standard deviation  $\sigma_0 = 2.42$  come from some systematic error due to the fitting procedure. The process that causes

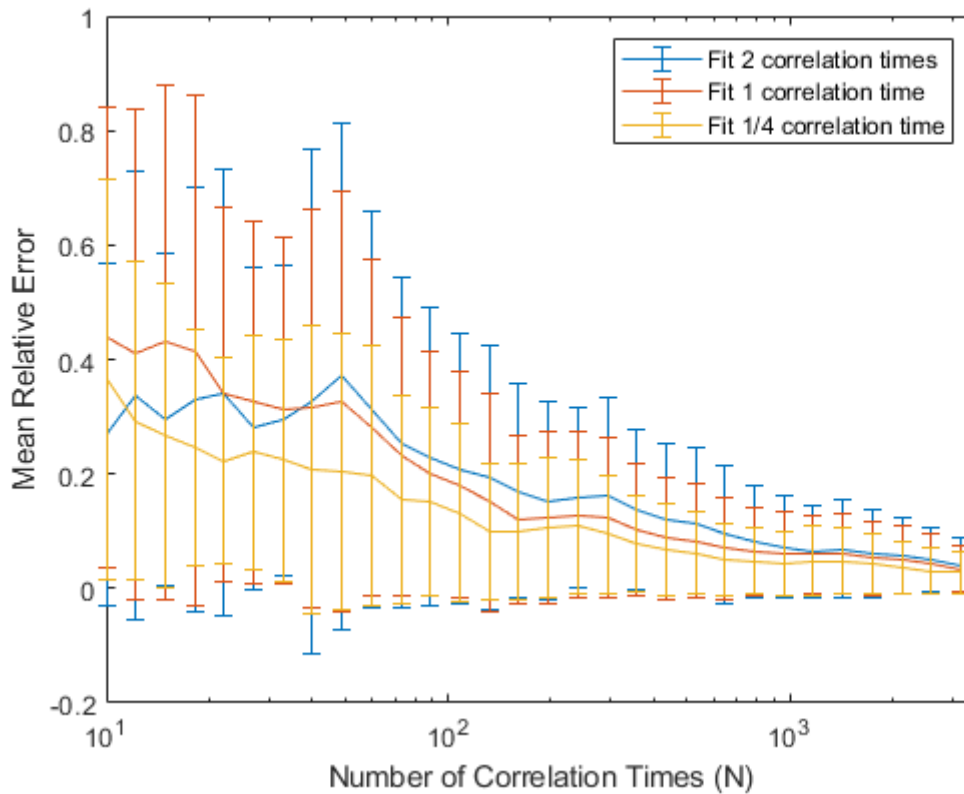


**Figure 3.6: Systematic error due to fitting decreases with shorter fitting times.** 30 independent simulations were done to obtain the simulation data. Cantilever specifications were:  $Q = 1000$ ,  $k = 1e6Nm^{-1}$ ,  $m = 1kg$ ,  $f_0 = 159Hz$ .

this deviation is unclear. We choose our estimated systematic error to be  $\epsilon_0 + \sigma_0$ . Then, in the range  $N = 100 - 3000$  for which we typically measure, the actual error will be smaller than our estimated error for 68% of the time. Next to the averaging time, a second parameter influences the

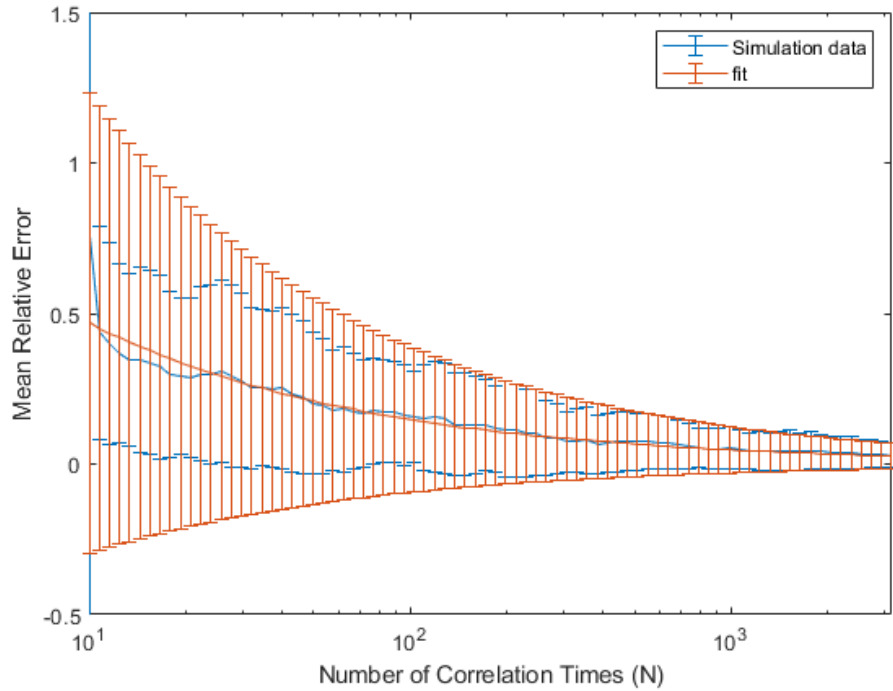


**Figure 3.7: Error dependence on number of correlation times.** The error on the determination of the Q-factor decays as  $\frac{1}{\sqrt{N}}$ . 30 independent simulations were done to obtain the simulation data, fitting was done for a length of  $\frac{\tau}{4}$ . Cantilever specifications were the same as in figure 3.6. Fits for both  $\epsilon_0$  and  $\sigma_0$  were done with the formula from equation 3.8, using Levenberg Marquardt algorithm.

accuracy of the Q-factor measurement. White noise on the measurement apparatus will decrease perceived correlation times. This consistent underestimation of the Q-factor was simulated by varying the  $SNR_{res}$  of the signal. It was found empirically that not only the  $SNR_{res}$ , but also the Q-factor and resonance frequency influence this error as not only the height, but also the width plays a role. It is clear from figure 3.8 that this deviation is not significant with respect to the error in figure 3.7 when the following criterion is satisfied:

$$SNR_{res} > 1000 \times \frac{Q}{f_0^2} \quad (3.9)$$

When this minimum  $SNR_{res}$  is computed for our systems specifications

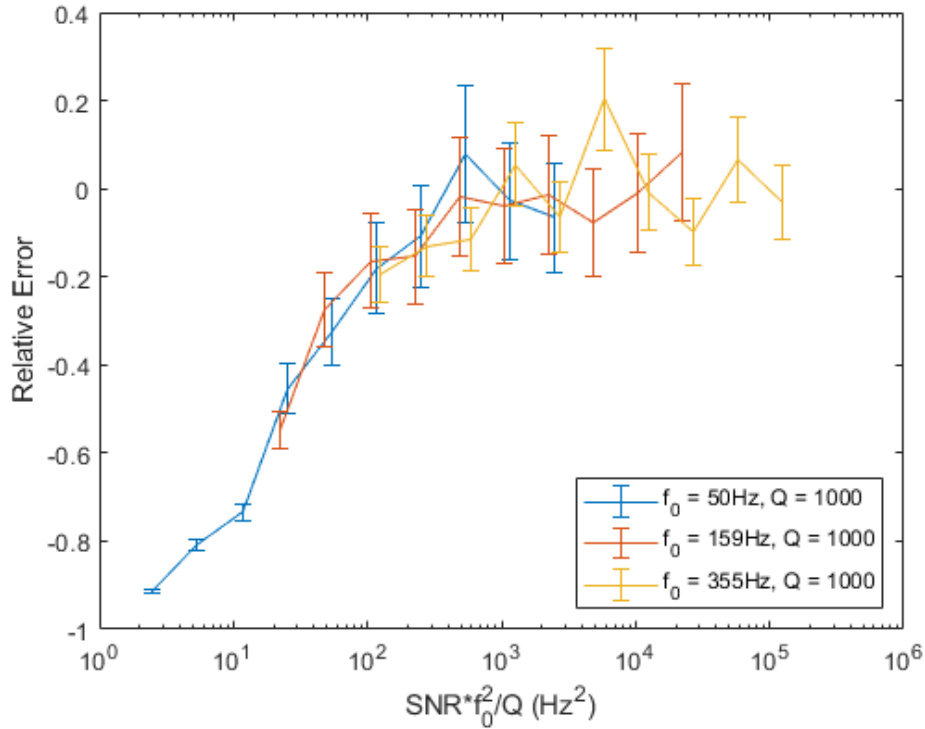


**Figure 3.8: Systematic error on  $Q$ -factor determination due to apparatus noise.** The  $Q$ -factor is systematically underestimated due to white noise on the apparatus at low  $SNR$ . Here, the dependence on the square of the resonance frequency is visualized. Similar simulations were done while varying the  $Q$ -factor. Data was simulated with different resonance frequencies and  $Q$ -factors, each having  $N = 3000$  correlation times.

( $Q \approx 1 \times 10^5$ ,  $f_0 = 5400\text{Hz}$ ), it can be concluded that no significant effects are taking part for an  $SNR_{res}$  above 3.4. In our experiments the  $SNR_{res}$  is typically found to be of order 500, rendering these effects negligible.

### Energy Measurement Corrected for $Q$

Now that we have discussed energy and  $Q$ -factor measurement and gained insight in their limitations, it is possible to simulate the predictions of 2.30. A multitude of cantilever signals is simulated, differing both in driving force noise and in  $Q$ -factor. For the driving force noise we use equation 2.20 meaning the force noise scales with  $\frac{T}{Q}$  and simulate a wide array of

temperatures. For the Q-factor we choose a decreasing relation with respect to temperature, one that is often observed in a true experiment (albeit the Q-values being much smaller here to save computation time). After the simulation of the signal, both energy and Q-factor measurements are done for all temperatures. In figure 3.9 three results from this simulation can be seen.

First, the linear relation between the input temperature is confirmed (bottom right), similar to figure 3.5. However, in this measurement, the Q-factor changed with temperature, altering both the input noise and the output energy, exactly canceling each other. Second, the Q-factor measurement accurately reproduces the input Q-factor within the estimated error.

### 3.3.5 Position to Voltage Conversion

Now that we are convinced that the data processing and Q-factor analysis works properly for a simulated signal, we can shift our focus to a more experimental problem. In reality, not the exact position is measured, but only a voltage that scales with the position:

$$V = \frac{\partial \langle V \rangle}{\partial x} x + V_{noise}(t) = u_x x + V_{noise}(t) \quad (3.10)$$

where  $V$  is the output voltage and  $V_{noise}(t)$  is the white noise sources of the apparatus that was added in figure 3.3 and has the property:  $\langle V_{noise} \rangle_t = 0$ . Also, we have defined the conversion factor  $u_x$ , describing the coupling between position and output voltage. Evidently, the quantity we call  $E_{cantilever} = \frac{1}{2} k x^2 \propto V^2$  is actually measured as a square of the output voltage. To estimate the absolute value of an excess force noise contribution from data as in figure 3.9, it is necessary to exactly compute this proportionality. There are two ways of determining the conversion factor, just from acquired data.

To measure the conversion factor, we utilize a graph as displayed in figure 3.9, a linear fit is done and using equation 2.30  $u_x$  is given by:

$$u_x = \sqrt{Z \frac{k}{k_B}}, \quad (3.11)$$

where  $Z$  is the derivative of  $\langle \frac{V^2}{Q} \rangle$  with respect to  $\frac{T}{Q}$ .

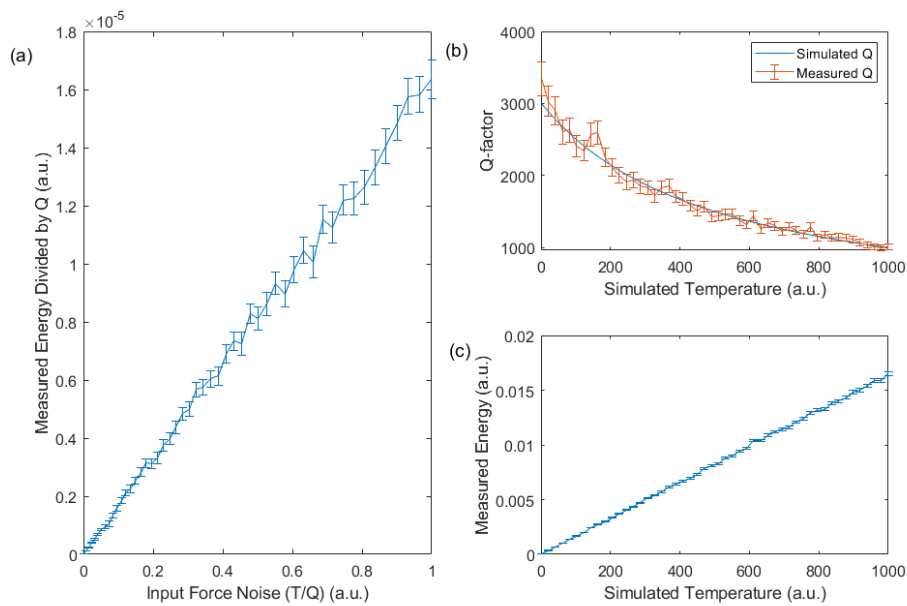


**Figure 3.9: Energy divided by  $Q$  vs. input force noise for simulation data.** *b)* For this measurement a decreasing  $Q$ -factor for higher temperatures was simulated. The measured  $Q$ -factors using the autocorrelation function are plotted on top, good agreement is observed (within error bars). *b)* The measured energy (which scales as  $Q$  with respect to the input noise) is plotted with respect to input temperature (which also scales as  $Q$  with respect to the input noise). The two scalars cancel out and we observe linear behaviour. *a)* The linear relation is still maintained when we plot the input force noise on the x-axis and energy divided by  $Q$  on the y-axis. The error bars are caused for the greater part by the error in  $Q$ -factor determination. The measurement was done using 30 simulations of  $N = 10000$  correlation times each, using previous cantilever specifications.

### 3.3.6 Computing the Excess Noise

When  $u_x$  is determined, equation 2.30 can be rewritten to give an expression for the excess noise:

$$S_{F_{Excess}} = \frac{y_0}{Z} \frac{4kk_B}{\omega_0}, \quad (3.12)$$

where  $y_0$  is the offset in  $V^2$  and  $Z$  is the slope in  $\frac{V^2}{T}$  as in equation 3.11. This expression is identical to the one found by Vinante et al. [10].

# Chapter 4

## Results

### 4.1 Measurement Overview

Measurements in the cryostat are done in runs, a certain period for which the cryostat is cooled down. These runs typically last anywhere between 2 weeks and several months. Here, we present the results of measurement runs 42, 43 and 44, which were performed between September 2018 and April 2019. Runs 42 and 43 focused primarily on the mechanical influences on the cantilever energy. After adjustments were done to reduce mechanical noise in the cryostat, our focus shifted to the influence of the sample temperature on the cantilever, which seemed to have a bigger impact on the energy than the mechanical noise.

In section 4.2 we describe a CSL measurement from run 43 in which we happened to suffer little from external mechanical vibrations and the cantilever had a lower coupling to the environment, attributed to its favourable position with respect to the pick-up loop. In section 4.3, we describe the actions that were taken to reduce the mechanical noise on the cantilever, leading to significantly lower cantilever energies. In section 4.4 we delve deeper into apparent defects in the quality of data sets caused by the influence of the environment, possibly driven by a coupling to a second heat bath.

## 4.2 CSL Measurement Run 43 (17-12-2018)

### 4.2.1 Cantilever Energy

As described in section 3.2.1 a typical CLS measurement is done by performing a temperature sweep. In the current data set (night of 17 on 18 December) the mass 3 temperature was varied between the following values:  $T = \{20, 34.2, 58.5, 100\}$  mK, each temperature being held constant for two hours. The temperature and the motion of the cantilever were continually measured.

As predicted by equation 2.24, the cantilever signal has a Lorentzian shape around its resonance frequency. To show this characteristic, we can perform a FFT and obtain the noise spectrum, as can be seen in figure 4.1. An interesting property of the ladder cantilever can immediately be observed, namely the temperature dependence of its resonance frequency. The peak is clearly shifted to higher frequencies at lower temperatures. As we will find out in section 4.4 this shift is actually not caused by the mass 3 temperature to which the resonator is attached, but by the sample temperature, illustrating the cantilevers interaction with the environment. Important here is to notice the reduction of the surface underneath the Lorentzian at lower temperatures. This surface scales with the energy of the cantilever (as dictated by the transfer function and input noise in equation 2.27) and is actually the property that is measured with the digital lock-in. Also, an increase in Q-factor at lower temperatures can be seen, as higher Q-factors yield a smaller FWHM. To quantify the cantilever energy (i.e. the surface under the Lorentzian), we use the digital lock-in as described in section 3.3.2 at the cantilever energy and merge the files according to 3.3.3. In this way, we gain insight in the the cantilever energy in the time domain, as can be seen in figure 4.2 where the processed data is plotted. Note how the cantilever energy grows with increasing temperature. Next, the cantilever energy is plotted with respect to the mass 3 temperature, shown in figure 4.3. The expected linear behaviour is observed, except for the 20 mK data point, which shows saturation effects. Therefore, this data point is omitted from the data set in further analysis. Saturation effects are examined in more detail in section 4.4.

### 4.2.2 Excess Noise

To calculate a figure for the excess noise, both axis of figure 4.3 have to be divided by the Q-factor, so that a constant offset emerges. The Q-factor is calculated according to the protocol explained in 3.3.4 and its dependence

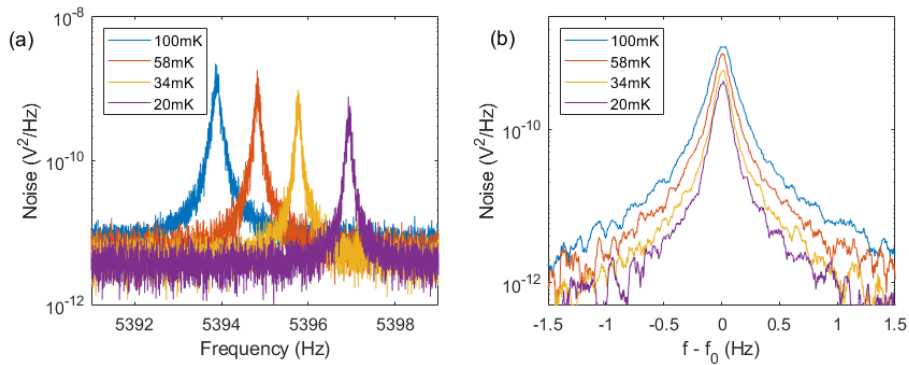


**Figure 4.1: Cantilever noise spectra for different cantilever temperatures.** a) Four spectra of the SQUID voltage output (squared) around the cantilever resonance frequency (90 minute average). Lowering of the cantilever energy (surface underneath the Lorentzian), as well as a shift in resonance frequency can be seen. The second is due to influence from the environment. b) The same spectra are plotted, corrected for their slightly different resonance frequencies and noise floor magnitudes (which are subtracted). Both a decrease in cantilever energy and an increase in  $Q$ -factor ( $\approx f_0 / \Delta f$ ) can be seen for lower temperatures. The data was smoothed with a moving mean with a bin size of 0.05 Hz.

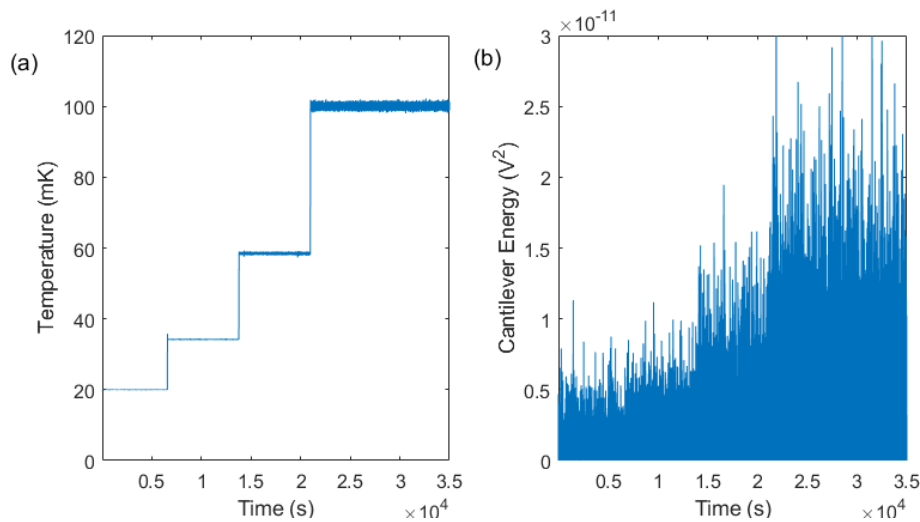


**Figure 4.2: Measured mass 3 temperature (mK) and cantilever energy in ( $V^2$ ).** a) The temperature of mass 3 (to which the cantilever is thermally anchored) is held constant at different temperatures. b) The cantilever energy is measured continually with the digital lock-in and temperature and energy measurement are synchronized according to section 3.3.3.

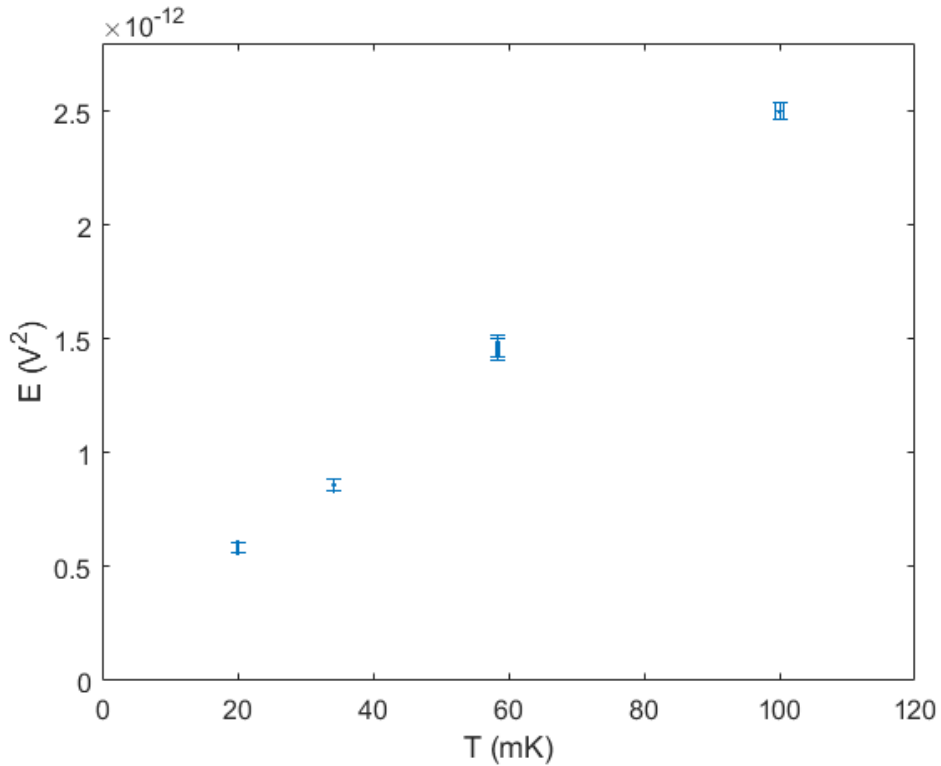


**Figure 4.3: Cantilever energy in  $V_{SQ}^2$  versus bath temperature.** Every data point represents an average over 30 minutes of thermal noise.

on the bath temperature is plotted in figure 4.4. The measured Q-values for our nanoladder cantilever are equivalent to the maximum values described in reference [18] at 100 mK. At lower temperatures, the Q-factor increases to a maximum value of  $7.2 \pm 1.3 \times 10^4$  at 20 mK. Interestingly, values for the Q-factor are not consistent across data sets for which the cantilever position is altered. Often, lower values are measured, attributed to a secondary dissipation channel, an observation that will be reviewed in more detail in section 4.4.

In figure 3.9 a plot of the cantilever energy divided by Q versus the bath temperature divided by Q can be seen. As the uncertainty in the determination of the Q-factor is much larger than the error in the cantilever energy, one would expect this error to be dominant in propagation. However, because both axes scale with Q, an error in Q only shifts the points towards or away from the origin. Thus, we can plot the data without accounting for the error in Q, adding two extra points: one for which Q is one standard deviation bigger than expected and one for which it is one

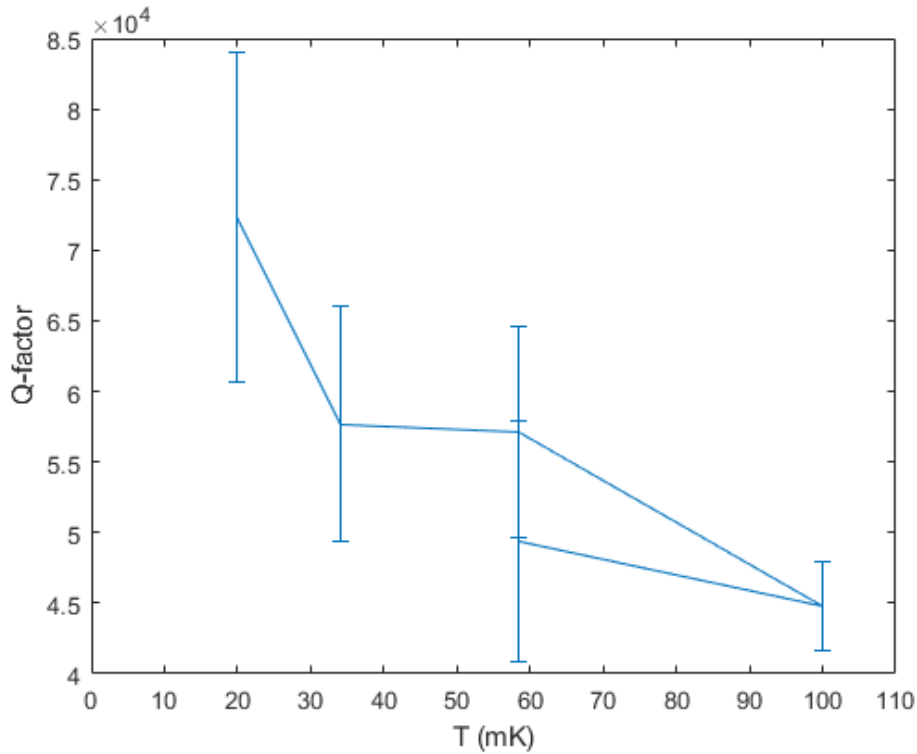


**Figure 4.4: Effective  $Q$ -factor with respect to temperature, measured using the autocorrelation function.** This  $Q$ -factor determination was done on the same data set displayed above. The error bars are determined according to equation 3.8, with  $N \approx 1500$ .

standard deviation smaller. These  $Q$ -error correction points then show the shift that is to be expected due to measurement error in  $Q$ .

A linear fit is done through the data points, the 20 mK point being for the reasons explained earlier. The fit yields a slope  $Z = 2.497 \pm 0.003 \times 10^{-11} \text{ V}^2\text{K}^{-1}$  and offset  $y_0 = 5.084 \pm 3.973 \times 10^{-20} \text{ V}^2$ .

Next, the excess force noise can be estimated using equation 3.12, resulting in the following value:

$$S_{F_{\text{excess}}} = 2.02 \pm 1.58 \times 10^{-40} \text{ N}^2\text{Hz}^{-1} \quad (4.1)$$

and we can say with 95% certainty that the excess force noise due to CSL is smaller than  $5.18 \times 10^{-40} \text{ N}^2\text{Hz}^{-1}$ .

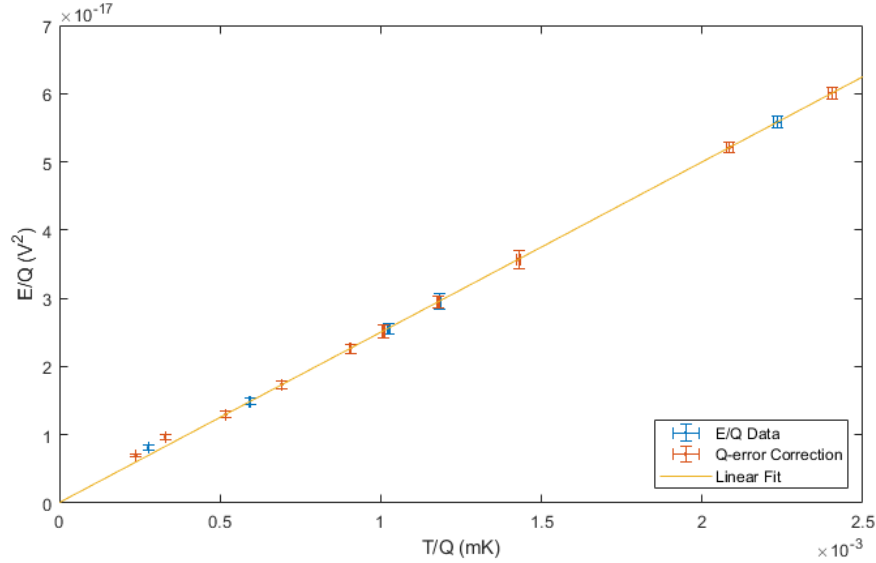


**Figure 4.5: Energy versus temperature plot, divided by  $Q$  and corrected for  $Q$  error.** The red points indicate the upper and lower bound to measured  $Q$ -values for every blue data point. The 20mK data point was omitted for the linear fit.

### 4.2.3 Continuous Spontaneous Localization Bounds

Now, an upper bound for the CSL parameter  $\lambda_{CSL}$  as a function of the correlation length  $r_C$  can be computed using the measured excess force noise. When we compare our measured excess force noise to that found by Vinante et al. [10], we find that our offset is almost four orders of magnitude smaller than theirs ( $1.87 \times 10^{-36} \text{ N}^2\text{Hz}^{-1}$ ), predominantly driven by the spring constant of our resonator, which is four orders of magnitude smaller. However, we must be prudent not to jump to conclusions about measured CSL parameters. In their setup, a much bigger magnet was used and hence a bigger CSL noise is expected. To include the radius of the sphere in our calculation and arrive at an expression for the maximum  $\lambda_{CSL}$ , we refer to equation 2.12 where the excess force noise upper bound with 95% is used. The result is plotted in figure 4.6. Our measurements yields a new upper bound for  $\lambda_{CSL}$  in the range  $r_C < 1.6 \times 10^{-6} \text{ m}$  and has specific values of  $1.6 \times 10^{-9} \text{ s}^{-1}$  for  $r_C = 1 \times 10^{-7} \text{ m}$ , which is the standard choice in CSL theory [3]. This is an improvement of a factor 12 and almost completely rules out Adler's proposal for this value of  $r_C$  [9], even without taking into account the contribution from the cantilever to CSL noise.

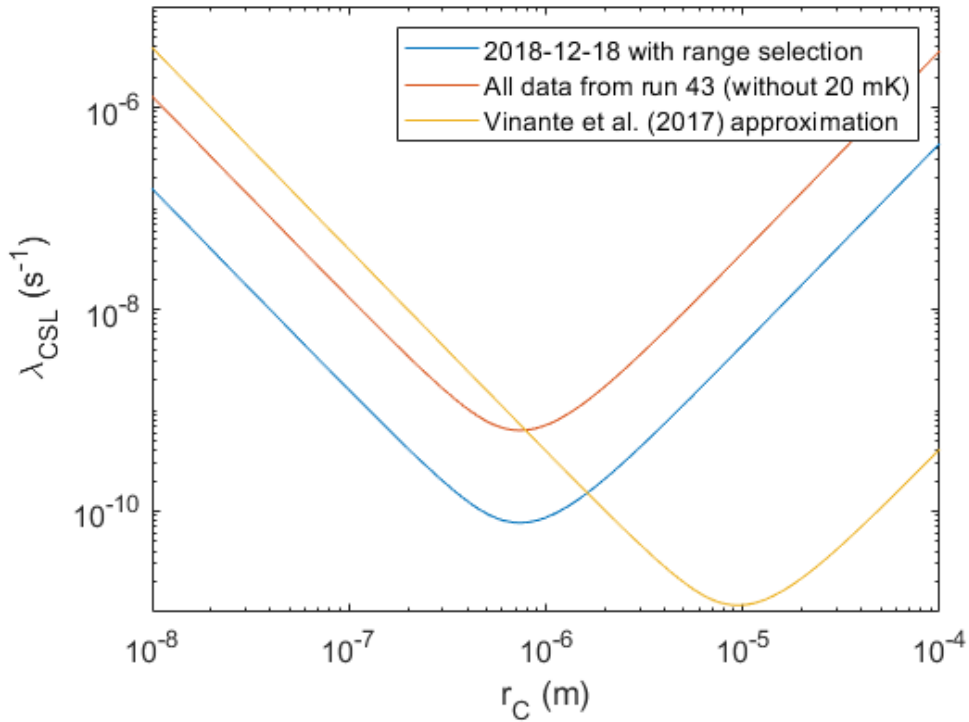


**Figure 4.6:** Maximum value of CSL parameter  $\lambda_{\text{CSL}}$  as a function of  $r_C$ . Our data sets bounds on  $\lambda_{\text{CSL}}$  approximately a factor 12 lower for  $r_C < 1.6 \times 10^{-6}$  m. For now, the effect of the mass of the cantilever itself has not been taken into account

#### 4.2.4 Data Disclaimer

##### Variability of Data

The results presented in this chapter are derived from one data set that sets exceptionally low upper bounds, with respect to comparable measurements. Here, we explain our motivation for choosing this data set and present other data that sets less impressive upper bounds. In this way, we try to provide an honest and transparent frame for our results.

##### Choice of Data Set

In run 42, significant mechanical vibrations still reached the experiment, rendering the results meaningless. This was improved upon and in run 43 and 44 mechanical vibrations no longer posed an issue, as is explained in section 4.3. Due to the cantilever's favourable position above the pick-up

loop in run 43 compared to run 44, saturation effects were less prominent. Therefore, we chose to analyze the temperature sweeps that were done in run 43 in more detail. The table below shows the 95% excess force noise and the standard deviation on the measurement. The ultralow upper bound from the 2018-12-17/18 data set predominantly owes its quality to the small standard deviation in the determination of the offset, which is an order of magnitude smaller than the standard deviation of other measurements. Hence, we conclude that it is extremely important for this experiment to have a very stable setup, robust against parameter drifts (e.g. slight position drift changes the coupling which reduces consistency among data points) and to measure a large spread in temperature data points above the saturation temperature to decrease the error margin.

Measurement Date	$S_{F_{excess}}$ 95% ( $N^2Hz^{-1} \times 10^{-39}$ ) (without data-selection)	$\sigma$	$S_{F_{excess}}$ 95% ( $N^2Hz^{-1} \times 10^{-39}$ ) (with data selection)	$\sigma$
Combined	4.43	1.30	4.98	2.45
2018-12-15/16	10.1	2.56	11.2	17.9
2018-12-17/18	1.33	2.03	0.518	0.165
2018-12-18	8.43	2.14	7.61	4.68

If we choose not to isolate the data set from 2018-12-17/18 and instead combine all the data from this position we measure a higher excess force noise of  $S_{F_{Excess}} = 4.43 \times 10^{-39} N^2 Hz^{-1}$ , resulting in the red curve in the CSL parameter space in figure 4.6. To obtain this value no data selection is applied, only the data below 20 mK is omitted. This is still a respectable result, as it offers a slight improvement with respect to the best measurement so far in the Oosterkamp group [9].

### Selecting Data Within Data Set

The data points that are plotted in figure 4.5 are averages over selected ranges in the data set. Data selection within a data set is based on two requirements: mechanical disturbance to the setup should be minimal and both the mass 3 temperature and sample temperature should be stable so that the cantilever is thermalized properly. For the first requirement, nighttime measurements are preferred over daytime measurements as deviations from the set temperature are more frequent during the day, as can

be seen in figure 4.7. This increase is attributed to an increase in mechanical disturbances to the setup, as is explained in section 4.3. To satisfy the thermalization requirement, only parts of the data are selected where the mass 3 temperature is constant. Also, we demand that the difference between the mass 3 temperature and the sample temperature is stable. Data less than 600 seconds before a major temperature change (e.g. from 20 mK to 34.2 mK) is not taken into account, because the temperature change causes the cantilever peak to shift in the frequency domain, creating a mismatch between the lock-in frequency and the actual resonance frequency for that specific 10 minute file. As the lock-in bandwidth is typically much larger than the width of the peak, this is no problem for minor temperature changes and accompanying frequency shifts.

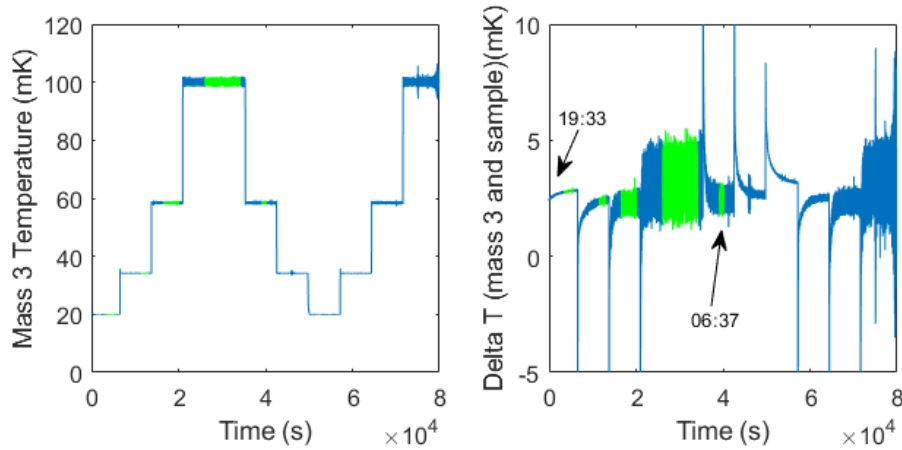


**Figure 4.7:** Data selection is done by demanding that both mass 3 temperature and sample temperature are stable. a) The complete data set of the temperature sweep covers the night and day of the 17<sup>th</sup> and 18<sup>th</sup> of December. b) The difference between the mass 3 and sample temperature exemplifies that it takes some time for the sample to reach thermal equilibrium. For the result in equation 4.1 only data that is shaded green is used.

## 4.3 Mechanical Noise

### 4.3.1 Mechanical Disturbance

In run 42 we investigated the influence of mechanical noise on the cantilever energy. In earlier runs it was noticed that mass 3 seemed to warm up in the morning during week days. It was hypothesized that this warming was caused by mechanical vibrations of the cryostat, which might

warm the springs of the mass spring system as they are stretching to damp the movement. Because our new post-processing method of analysis allows us to continually observe the cantilevers energy, the opportunity arose to measure whether the cantilever was also excited during these mornings. In figure 4.8 the warming of mass 3 can be observed around 07:00, around traffic rush hour and when construction work might start. From this hour, the cantilever energy increases as well, seemingly more than should be expected from the minor temperature rise. To prove that the observed heating is caused by mechanical vibrations, a geophone was placed on top of the cryostat that measured vibrations of up to 100 Hz. The measured mechanical noise for 1 – 10 Hz is also shown in figure 4.8 for the same morning. A remarkable correlation between the temperature rise and mechanical noise can be seen.

Now, we investigate if this increased noise also influences the cantilever energy directly. In order to do this, we calculate the relative cantilever temperature by dividing the temperature of the cantilever by the temperature of the heat bath. Then, we plot the relative temperature versus the measured low frequency noise in figure 4.9. We would expect this ratio to be unity if the cantilever felt no other influence than the thermal bath. However, the cantilever temperature is 80% higher than the bath temperature during the quiet hours of the night and its temperature increases to three times the bath temperature when the mechanical noise intensifies. Thus, we can conclude that mechanical noise directly heats the cantilever.

In order to understand how the cantilever may be excited in this way we examine the experimental setup again. As the mass-spring system is low pass filter designed to block high frequency vibrations, it is expected that low frequency noise reaches the experiment. However, since the cantilevers resonance frequency is at 5.4 kHz this noise should not influence the experiment. It was computed by de Wit et al. [19] that mechanical noise decays with 120dB per decade above the cutoff frequency (4 Hz), thereby rendering it in principle impossible for high frequency noise to penetrate into the experiment and excite the cantilever.

There are two ways high frequency noise can still reach the experiment. The first possibility is that there exists a shortcut, letting high frequency vibrations pass by the mass spring system and directly to the experiment. The second is that there is some mechanism converting low frequency noise into high frequency noise at the bottom of the mass-spring system.

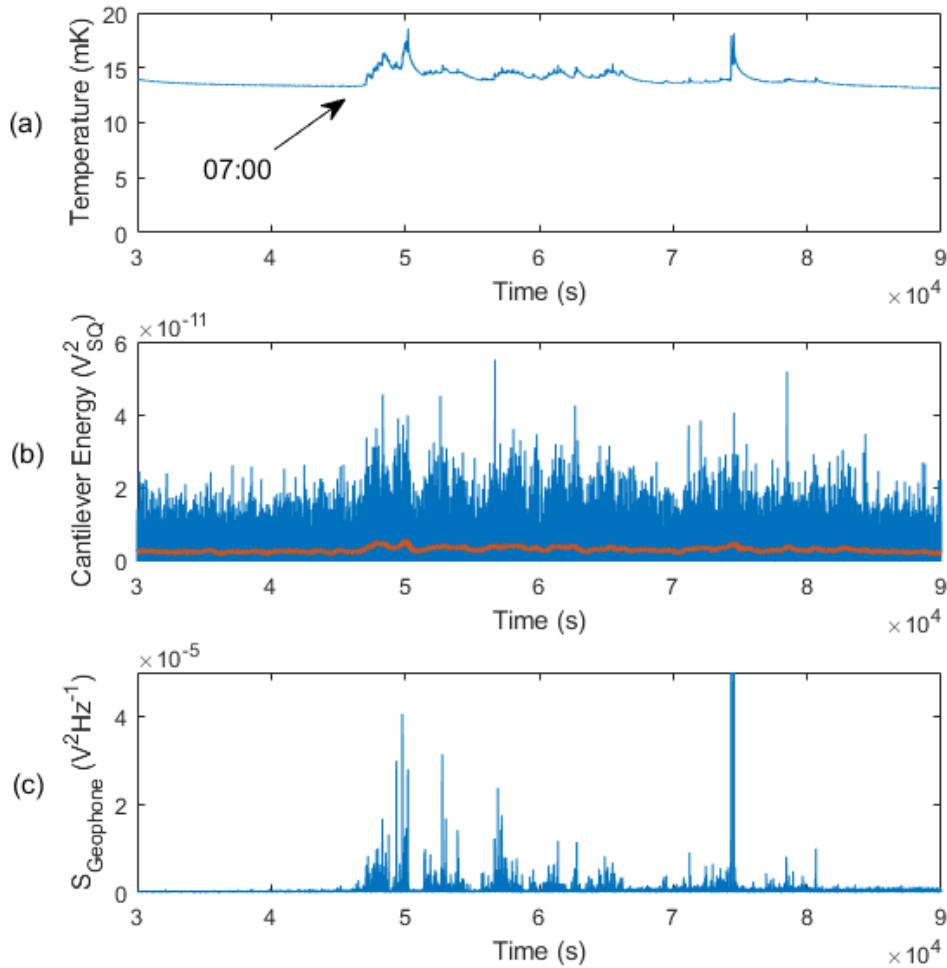


**Figure 4.8: Both the mass 3 temperature and the cantilever energy increase at the start of office hours.** a) Around 07:00, increases in mass 3 temperature were observed. b) The cantilever energy was seen to increase more than expected from purely thermal excitation. Therefore, it was thought that the cantilever was excited mechanically during these mornings. c) The mechanical noise in the range (1 – 10Hz) also increases in the morning of this data set. SQUID and temperature data is from 2018-10-25/26 (Thursday on Friday, run 42).

### 4.3.2 Improvements of the Mechanical Isolation

To decrease the chance of high frequency noise reaching the experiment via a shortcut, we investigated a possible shortcut that was present in the

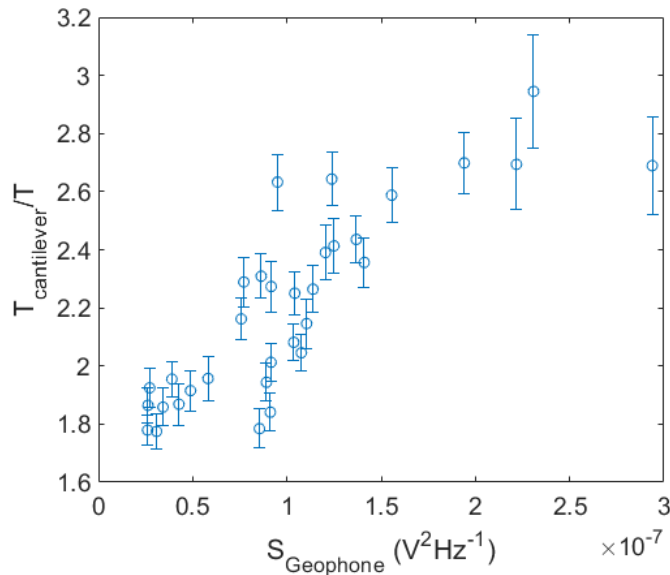


**Figure 4.9: An increase in vibrational noise measured on the cryostat leads to an increased cantilever energy.** Clearly, the cantilever is excited mechanically due to external vibrations. This is either caused by a shortcut in the mass spring system or a mechanism which converts low frequency noise into high frequency noise. Datapoints are 30 minute average from the data set presented in figure 4.8.

setup. As can be seen in figure 4.10, the cables to the experiment were loosely tied to the mass spring system in run 42. It was posed that these cables might transmit high frequencies as they are not very well anchored to the mass-spring system. Bundle cables were designed to get rid of this problem, joining all cables together and securing it tightly to the masses. The twenty or so cables were plugged into these bundle cables at mass 3 and they were meandered up together, making sure that they were not under any mechanical strain. In run 44, clamps were added to anchor the cables even more rigidly to the masses. To test if the bundle cables resolve the heating observed in figure 4.9, we would have liked to replicate the experiment shown in figure 4.8. However, during run 43 and 44 the geophone was not connected as we had switched to a vibration sensor inside the cryostat based on a piezoelectric element. To be able to still compare the effects of mechanical noise in the two runs we resort to an interesting fact that was observed in run 42. Namely, we investigated how the the low frequency signal of the SQUID (1 – 10 Hz), was effected by the inbound mechanical noise in the morning of figure 4.8. When we plot the low frequency noise on the SQUID versus the mechanical noise, a clear

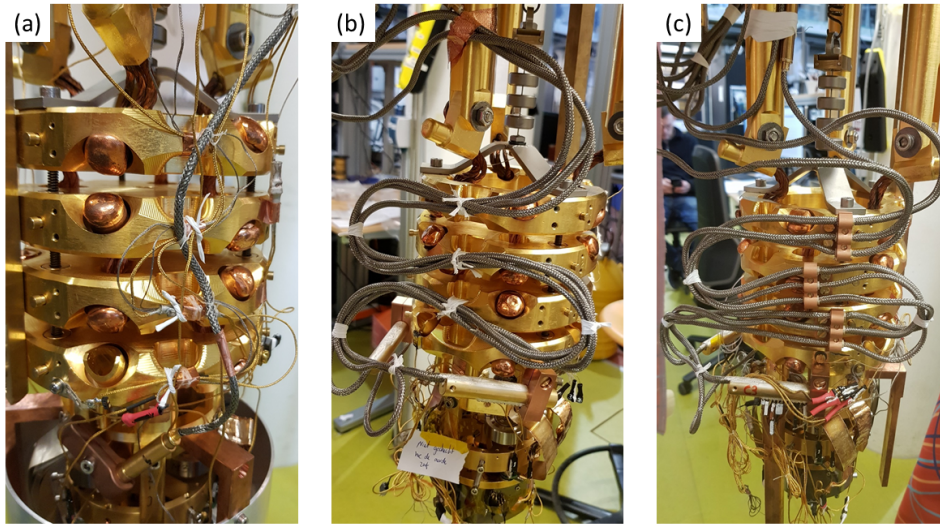


**Figure 4.10:** Bundle cables were designed for the mass-spring system to get rid of a possible mechanical shortcut a) In run 42 all the cables that were connected to the experiment (20 or so) were attached individually to the masses using dental floss and PTFE tape. b) In run 43, bundle cables were introduced to get rid of this possible shortcut in the mass-spring system. c) In run 44, clamps were added to complete the improvements.

correlation is seen. We presume that this is caused by microphonics in the SQUID cable caused by the oscillating mass-spring system. Interestingly, the low frequency SQUID signal can thus be used as a measuring device for mechanical noise. The observed offset is either due to SQUID tuning or caused by the fact that the mass spring system might still be oscillating when the cryostat is not.

As we always record the entire SQUID signal, we can still get a measure for the magnitude of the mechanical noise by examining the low frequency components. In figure 4.12 the relative cantilever temperature is plotted with respect the low frequency mechanical noise measured with the SQUID. We correct for different SQUID tuning between runs, by assuming that the mechanical noise had a comparable magnitude between 04:00 and 06:00 in both runs. Two important conclusions can be drawn. First, the relative temperature of the cantilever lies significantly lower after the installation of the bundle cables. Second, the relative temperature no longer increases as a function of low frequency mechanical noise.

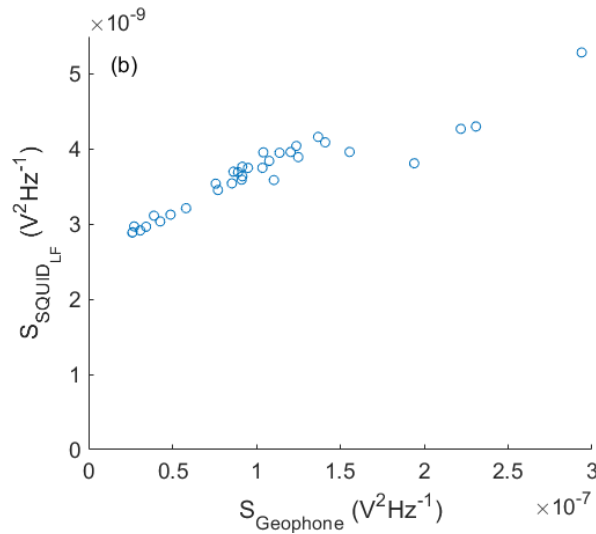


**Figure 4.11: Increases in the (low frequency) mechanical noise can also be seen in the low-frequency SQUID signal (1 – 10 Hz). In this way, the low frequency SQUID noise can be used to measure mechanical noise acting on the mass-spring system.**

We attribute these improvements to the introduction of the bundle cables as this was the only significant modification that was done in run 43. We think that the measured low frequency noise is part of white noise, delta peak, ‘bumps’ against the cryostat. Without the bundle cables in place, the high frequency components of these bumps were able to bypass the mass spring system through the experiment’s wiring and excite the cantilever. Thus, by the design and execution of the bundle cables we have significantly reduced the influence of mechanical noise on the experiment.

### 4.3.3 Pulse Tube Noise Reduction

Now that it has become clear that mechanical noise can have a detrimental influence on the experiment, we propose a way in which we can possibly further reduce this nuisance. Even though we are confident that sporadic high frequency noise no longer bypasses the mass-spring system, the possibility still exists for constant low frequency sources to affect the cantilever via an up-conversion mechanism. More concretely, it is hypothesized that the pulse tube, which is by far the biggest contributor to the low frequency noise, is constantly letting the mass-spring system oscillate. If this is the case, the copper elements of the suspension might be grinding

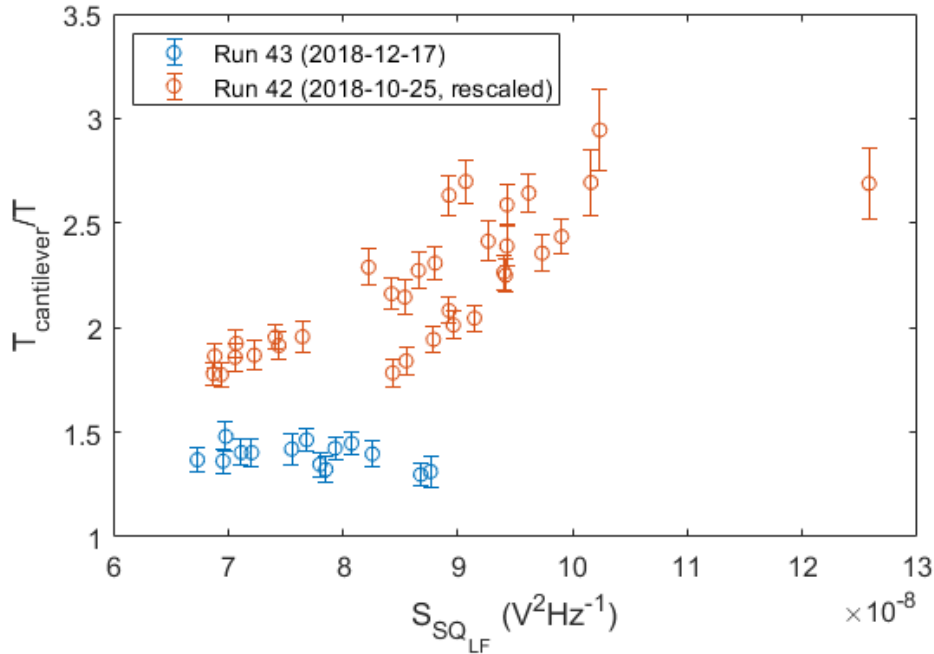


**Figure 4.12:** *The relative cantilever temperature is no longer affected by low frequency mechanical noise, attributed to the installation of bundle cables. The data from run 43 is taken from a Monday morning (2018-12-17), when the cryostat was at base temperature and similar heating to that in figure 4.8 was seen around 07:00. The data from run 42 is corrected for a different SQUID tuning, so that a proper comparison can be made.*

over each other, hereby creating high frequency noise.

To test this hypothesis, the pulse tube was turned off nine times for three minutes at a time. The cantilever energy was examined during these periods and compared to a two hour measurement from the same data set when the pulse tube was on. No significant fall in relative cantilever temperature was observed, as can be seen in figure 4.13.

Thus, we are skeptical that further improving our vibration isolation or lowering the mechanical noise input will lower the relative cantilever temperature below current levels. As the cantilever temperature is still found to be 50% too high around base temperature (15 – 20 mK), there must be another type of noise source at play. In section 4.4 we will uncover the mechanism that causes this extra unwanted heating.

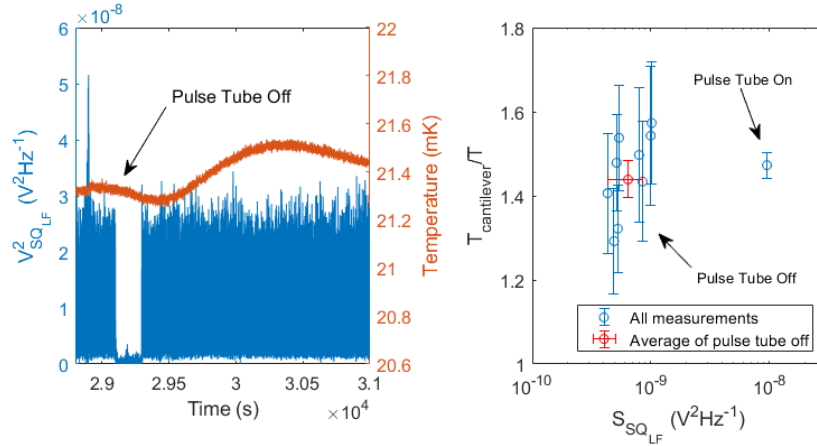


**Figure 4.13: Turning off the pulse tube does not further lower the relative cantilever temperature.** a) The low frequency energy of the SQUID can be seen to drop by an order of magnitude when the pulse tube is turned off. A maximum of three minutes is maintained as the cryostat will otherwise heat up too much. b) The three minute measurements are averaged and compared to the relative temperature when the pulse tube is on. Data is from run 44 (2019-02-23).

## 4.4 Energetic Coupling to the Environment

### 4.4.1 Saturation Behaviour

In all our data sets (especially in run 43 and 44) we see similar saturation behaviour as was observed by references [9] and [16]. At mass 3 temperatures below 30 mK the cantilever's temperature stops decreasing. Usenko et al. [16] attributed this behaviour to to be independent of the specific circumstances in the respective runs as the cantilever and its connection to mass 3 does not change.

We investigate the differences in saturation of the combined data from run 43 and an extensive temperature sweep from run 44. First, the same saturation fit as Usenko et al. used is applied:

$$V_{SQ}^2 = (ZT^n + Y_0^n)^{1/n}, \quad (4.2)$$

where  $V_{SQ}^2$  is the cantilever energy and  $Z$ ,  $n$  and  $Y_0$  are the free parameters. The steepness of saturation is determined by  $n$ ,  $Y_0$  is the saturation offset in  $V^2$  and  $Z$  has the same role as in equation 3.12, namely the conversion between temperature and voltage squared. Then, the saturation

temperature of the cantilever is computed:

$$T_0 = \frac{Y_0}{Z}. \quad (4.3)$$

Energy data and saturation fits can be seen figure 4.14. We observe a significant difference in saturation temperature for run 43 and run 44,  $22.1 \pm 1.0$  mK versus  $29.2 \pm 0.5$  mK, respectively. Also, the steepness of saturation seem to vary between runs, although they are consistent within error bars.

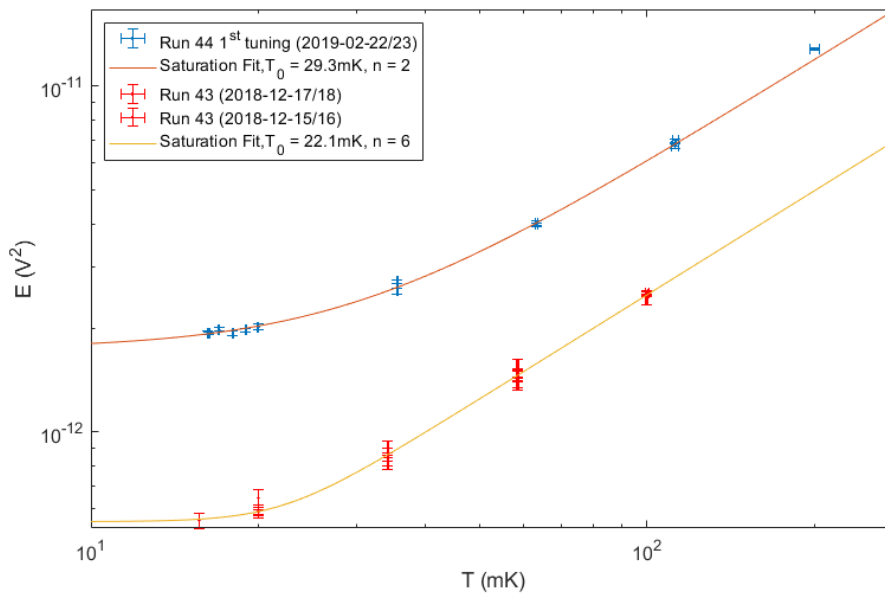


**Figure 4.14: The saturation temperature of the cantilever differs for different runs.** The cantilever saturates at  $29.2 \pm 1.0$  mK in run 44.  $n = 2.9 \pm 0.5$ . The cantilever saturates at  $22.1 \pm 1.9$  mK,  $n = 5.1 \pm 1.1$ . Data points above 120 mK are omitted, because our thermometry is no longer linear in this regime. There is insufficient data from the other positions in run 43 to do a proper fit of the saturation temperature.

Another significant difference between the specific runs can be seen when we compare Q-factors measurements. In figure 4.14, damping coefficients are plotted, showing a greater damping in run 44 for temperatures in the range 30 – 100 mK. The damping factors can from run 43 and 44 can be rewritten into Q-factors, of the order of  $5.3 \times 10^4$  and  $4.5 \times 10^4$ , respectively. In run 43, the damping factor reduces significantly for temperature below 20 mK, as is expected for the ladder cantilever [18] [? ]. That we do not see a similarly abrupt decrease in run 44 is attributed to the higher saturation temperature that was observed.

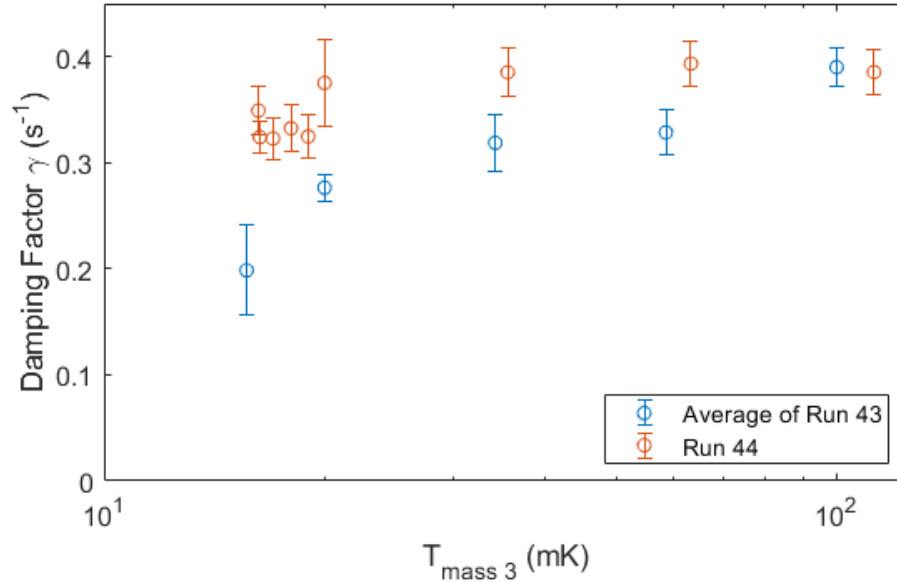


**Figure 4.15:** *The damping of the cantilever varies between runs, attributed to extra damping caused by stronger coupling to the environment. The damping factors are calculated according to equation 2.21. Data points are averages of Q-factor computations from the same data that can be seen in figure 4.14.*

The higher saturation temperature in combination with increased damping of the cantilever in run 44 leads us to hypothesize that saturation is not caused by limiting thermal conductance, but rather by a coupling to a (warmer) second heat bath on the detection chip. This coupling works as an (inverse) dissipation channel, increasing the damping. Furthermore, it is posed that the coupling strength is strongly dependent on the cantilevers position, explaining the differences between runs.

#### 4.4.2 Coupling to a Second Heat Bath

We pose that there exists a dissipative element on the detection chip, which has a limiting thermal conductance, thereby having a higher temperature than mass 3. This element couples into the experiment and acts as a second heat bath. We refrain from speculating about the exact nature of the element and its method of coupling to the cantilever. The purpose of this section is to demonstrate both the existence of the coupling and to show that we can exert some manner of control over the detrimental influence of this element on our experiment.

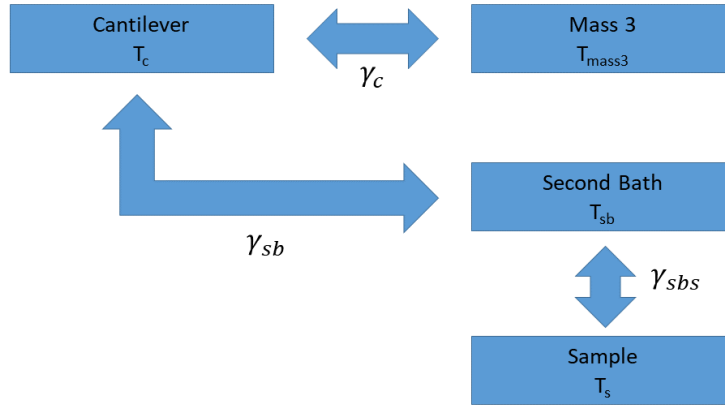


**Figure 4.16: Schematic of the proposed model for describing saturation behaviour.** It is posed that there exists some dissipative element on the sample, which warms both the cantilever and sample. The total damping of the cantilever is then its mechanical damping  $\gamma_c$  and a damping factor caused by the dissipative channel to the environment  $\gamma_e$ . In this model, the sample temperature  $T_s$  can be used to indirectly measure  $T_e$ . Also, by heating the sample,  $T_e$  can be increased.

In our model, the cantilever is not only coupled to the temperature of mass 3 but also to a temperature in its environment, thereby increasing its equilibrium temperature. The simplest model for this proposed system is that the cantilever temperature is a weighted mean of the two temperatures of the sources to which it is coupled to:

$$T_{cantilever} = \frac{\gamma_c T_{mass3} + \gamma_{sb} T_{sb}}{\gamma_c + \gamma_{sb}}, \quad (4.4)$$

where  $\gamma_c$  is the internal, intrinsic damping factor of the cantilever (in other words: the coupling to the mass 3 heat bath  $T_{mass3}$ ),  $\gamma_{sb}$  is the coupling to the second heat bath and  $T_{sb}$  is the temperature of this bath. A schematic drawing of the proposed model is seen in figure 4.16.

An important clue for proposing a coupling to a second heat bath, was that the saturation temperature seemed to be higher when the sample holder was warmer (an independent thermometer is present on the sample holder). If the second heat bath is situated on the detection chip, it should it should rise in temperature when the sample holder is heated. In order to verify this supposition, the temperature of the environment is

changed experimentally by heating the sample holder. During heating, the temperature of mass 3 remains constant, so if the cantilever were only coupled to the mass 3 thermal bath, its energy should not change.

However, from figure 4.17 it can be seen that the increased sample temperature (to 100 mK) increases the cantilever energy significantly (data from run 44). Saturation fits as in equation 4.2 are done on the data. The exponent is unchanged within error bars, but the saturation temperature is raised from  $29.6 \pm 1.0$  mK also seen in in figure 4.14, to  $40.2 \pm 0.7$  mK. Hence, the temperature of the sample holder, and thereby of the second heat bath, significantly influences the cantilever temperature.

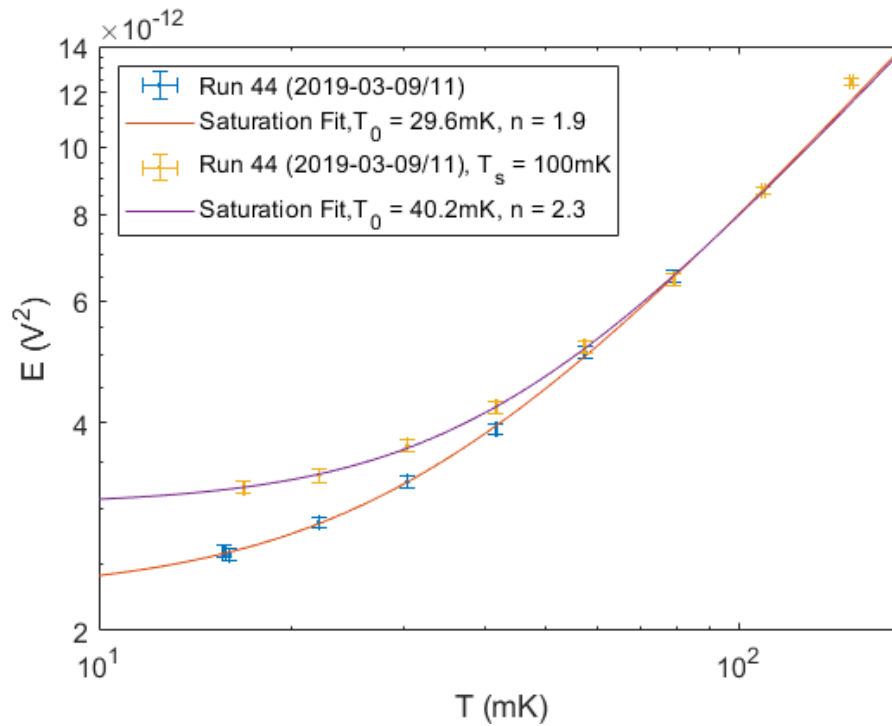


**Figure 4.17: Cantilever saturation temperature is dependent on the environment temperature.** When the sample temperature is increased to 100mK (normally it is 2 – 5mK above  $T_{mass3}$ ), the saturation temperature increases significantly. This indicates that the environment temperature is coupled to the cantilever temperature. Data is from run 44 (2019-03-09/11)

### 4.4.3 Coupling Mechanism

There are only two major differences that can be identified between runs: the cantilever's position with respect to detection chip and the SQUID tun-

ing. The second is done at the start of each run to maximize the signal to noise ratio of detection. To exclude that this tuning influences the coupling, in run 44, the SQUID was retuned while the cantilever remained in the same position. Both the steepness ( $n$ ) and the saturation temperature ( $T_0$ ) do not change when the SQUID tuning is altered. Therefore, we conclude that the coupling to the environment is solely determined by the cantilever's position and that this is the key driver that should explain the differences in saturation behaviour between runs.

Next we examine possible coupling mechanisms that are dependent on the cantilever's position. There are only two channels through which the cantilever can couple to its environment. One is its mechanical attachment to the cantilever chip. Via this channel the cantilever thermalizes with mass 3, but this channel is the same in every run. The other way of interacting with its environment is through the attached magnetic bead. This channel is governed by electromagnetic interactions and our flux measurement goes through this channel. When we look for a second coupling, the electromagnetic channel is the most obvious. Therefore, we examine several magnetic sources in the vicinity of the cantilever, which might couple in.

### Surface Spins

Wagenaar et al. [20] investigated the influence of surface spins directly coupling in to the cantilever, resulting in extra damping and frequency shift. This interaction is extremely short range and it is found that spin-cantilever interaction can be neglected for tip-surface distances bigger than  $2.5 \mu\text{m}$  [21]. However, the authors describe Q-factor changes occurring at least up to  $5 \mu\text{m}$ , which cannot be attributed to dissipation through the spins. In our experiments, the cantilever was  $4 \mu\text{m}$  above the surface in run 43 and at least  $3 \mu\text{m}$  for run 44. Therefore we can conclude that the cantilever was not coupled to the surface spins.

### Stray Fields from the SQUID-circuitry Transformers

Other magnetic components in the circuitry near the cantilever are the transformers between the pick-up loop and the SQUID. As these transformers have multiple windings, they might have a much stronger magnetic influence than the pick-up loop. However, as we know that these transformers are relatively far away (order 1 cm), we can ascertain ourselves that the cantilever is in the far field limit. Therefore, the coupling to these transformers should not be so strongly dependent on the cantilever's

position. Because we can already see major changes in the coupling when the cantilever is moved a few micrometers, the option of long range coupling to the transformers is discarded.

### Pick-up Loop

The most probable way of coupling to the magnetic bead is through the pick-up loop. In fact we know a coupling already exists as we can measure the cantilevers position through it. Also the coupling with the pick-up loop was measured to be 2.5 times stronger in run 44 than in run 43. If the cantilever couples to the second bath via the pick-up loop, we would expect that coupling also to be 2.5 times stronger. This is in line with the higher saturation temperature and extra damping seen in figures 4.14 and 4.15.

We propose two mechanisms that might lead to the damping of the cantilever in the SQUID circuitry. First, we propose that there is a resistor in the SQUID circuitry that dissipates a constant power. The Johnson noise from this resistor might then couple into the pick-up loop through the transformers and couple into the cantilever. The cantilever will then reach a thermal equilibrium with this resistance. This possibility does not explain the observed temperature dependent frequency shift.

The second possible mechanism was coined by Vinante et al. [10] for explaining the extra damping and frequency shift in their setup. The magnetic spring effect, which works in a similar way as the optical spring effect, is responsible for a force opposite the cantilevers movement. In their setup, feedback is applied to the cantilever, which alters the spring constant and the Q-factor. When the no feedback on the cantilever is applied (as in our setup), the extra spring constant from the magnetic spring effect becomes [10]:

$$k_{SQ} = J_{\Phi} \Phi_x^2, \quad (4.5)$$

where  $J_{\Phi} = \frac{dI}{d\Phi}$  is the responsivity of the SQUID and  $\Phi_x = \frac{d\Phi}{dx}$ . Naturally  $\Phi_x$  remains constant at a certain position, as it is only dependent on the position of the magnetic bead with respect to the pick up loop. Therefore, any low temperature increases of  $k_{SQ}$  must be caused by an increase in  $J_{\Phi}$ . This parameter is dependent on the working point of the SQUID, as this determines the induced current when one flux quantum enters the pick-up loop. This parameter is highly dependent on the SQUID tuning, but no significant difference frequency shift or saturation was observed for different SQUID tunings.

#### 4.4.4 Modelling Saturation Behaviour

Here, we propose a model that explains the saturation behaviour and can even replicate the differences seen between runs up to a certain level. In short, the model works as follows: first, we make an educated guess for the strength of the coupling to the second heat bath ( $\gamma_{sb}$ ), based on the measured Q-factors. When we have an estimation for  $\gamma_{sb}$ , the intrinsic damping  $\gamma_c$  can also be calculated by subtracting  $\gamma_{sb}$  from the total damping factor. Then, we use equation 4.4 to compute how the cantilever temperature behaves as a function of mass 3 temperature, using a logical choice for the temperature of the second heat bath  $T_{sb}$ .

As discussed in equation 4.4, the total damping of the cantilever is comprised of both the internal damping  $\gamma_c$  and its coupling to the second heat bath  $\gamma_{sb}$ . In figure 4.18 we do an educated guess for how the total damping factor is built up. A simple exponential fit is done through the data points, just to have a smooth function approximating the data. The 100mK data point from run 43 is omitted, as we are mostly interested in the saturation behaviour which takes place at lower temperatures.

The guess for the contribution of  $\gamma_{sb}$  is based on two observations: first, as we have observed in figure 4.15 the damping of run 44 is  $0.064 \text{ s}^{-1}$  higher than in run 43 (in the 30 to 100 mK range), we ascribe this difference to the stronger coupling to the second heat bath (i.e.  $\gamma_{sb44} = \gamma_{sb43} + 0.064$ ). Second, as described in section 4.4.3, we assume that the coupling is established through the pick-up loop and that the coupling to the second heat bath should scale with the coupling to the pick-up loop. The coupling in run 44 was 2.5 times stronger than in run 43, yielding the second condition:  $\gamma_{sb44} = 2.5\gamma_{sb43}$ . Solving the system of equations yields the values  $\gamma_{sb43} = 0.043 \text{ s}^{-1}$  and  $\gamma_{sb44} = 0.107 \text{ s}^{-1}$ , which are plotted in figure 4.18. For the behaviour of  $T_{sb}$  we choose a standard saturation behaviour, driven by a constant dissipated power and a heat conductance of silicon which scales as  $T^{-3}$ , as the second heat bath is located on the detection chip. We choose a saturation temperature of 50 mK for the second heat bath. This is reasonable, as de Wit found [17] that the RF wire, lying on the detection chip, saturates at 45 mK when only 1 nW is dissipated. The choice for  $T_{sb}$  is plotted in yellow in figure 6.3.

Next, we compute the expected cantilever temperature for run 43 and 44, using the estimated coupling from figure 4.18 and bath temperature from figure 6.3, using equation 4.4. The result is plotted in blue and red, respectively, in figure 6.3. Two distinct characteristics can be observed. First, the expected saturation temperature is lower for run 43, due to the lower coupling to the second bath. Second, the saturation is steeper in

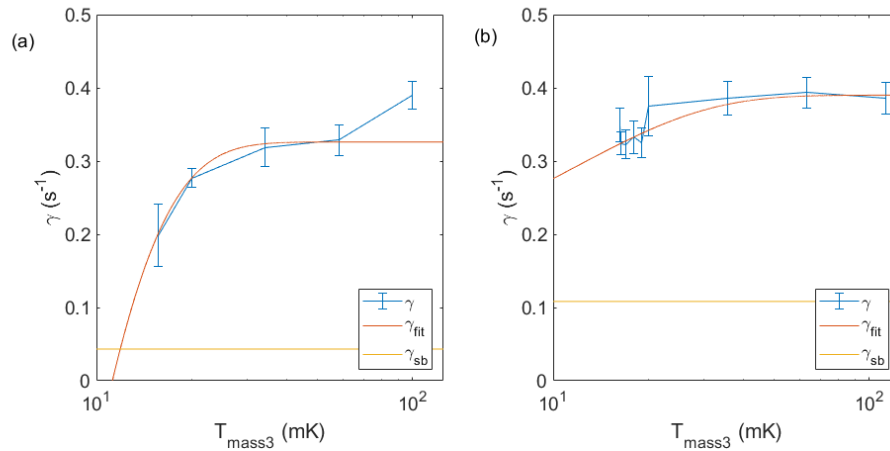


**Figure 4.18: A guess is done for the composition of the total damping factor for run 43 and 44.** a) For run 43,  $\gamma_{sb}$  was guessed to be  $0.043 \text{ s}^{-1}$ . b) For run 44,  $\gamma_{sb}$  was guessed to be  $0.107 \text{ s}^{-1}$ . Simple exponential fits were done to heuristically describe the data. Data is the same as in figure 4.15.

run 43 due to the quicker fall of of the internal damping, giving relative weight to the coupling to the second bath. Even though the cantilevers coupling to the second heat bath is constant, at low temperature the coupling to mass 3 decreases immensely (raising the Q-factor). Therefore, at low temperatures it predominantly takes on the temperature of the second heat bath.

Of course, figure 6.3 is only physical for temperatures above  $11 \text{ mK}$ , as the exponential fit predicts a negative non-physical coupling for lower temperatures. Also, we do not observe a rise in cantilever temperature at low temperatures in our data. This can easily be explained: the internal coupling of the cantilever acts as a feedback loop. When it cools down the Q-factor rises, decoupling the cantilever from mass 3 and taking on more the temperature of the second bath. This increase in temperature in turn lowers the Q-factor again and lets the cantilever dissipate its heat back to mass 3, cooling it again.

Interestingly, in a data set from Wagenaar (2015-02-13), a rising cantilever energy was seen at low bath temperatures ( $20 - 200 \text{ mK}$ ). This data was from an IBM style cantilever whose Q-factor is lightly less temperature dependent than that of the ladder cantilever. The rise in energy was unexplained so far, and could very well be caused by a similar mechanism as described above. However, the quality of the data set is bad and the cantilever and parts of the setup are different. Therefore, no conclusions can be drawn from the data, which can be found in the appendix.

The model described is by no means a fully quantitative description of the saturation behaviour witnessed in the different runs. However, it does model the saturation behaviour qualitatively and manages to replicate observed differences in both steepness and saturation temperature between runs. It does this based on only two assumptions: an educated guess for the coupling and a constant dissipation in the second heat bath.

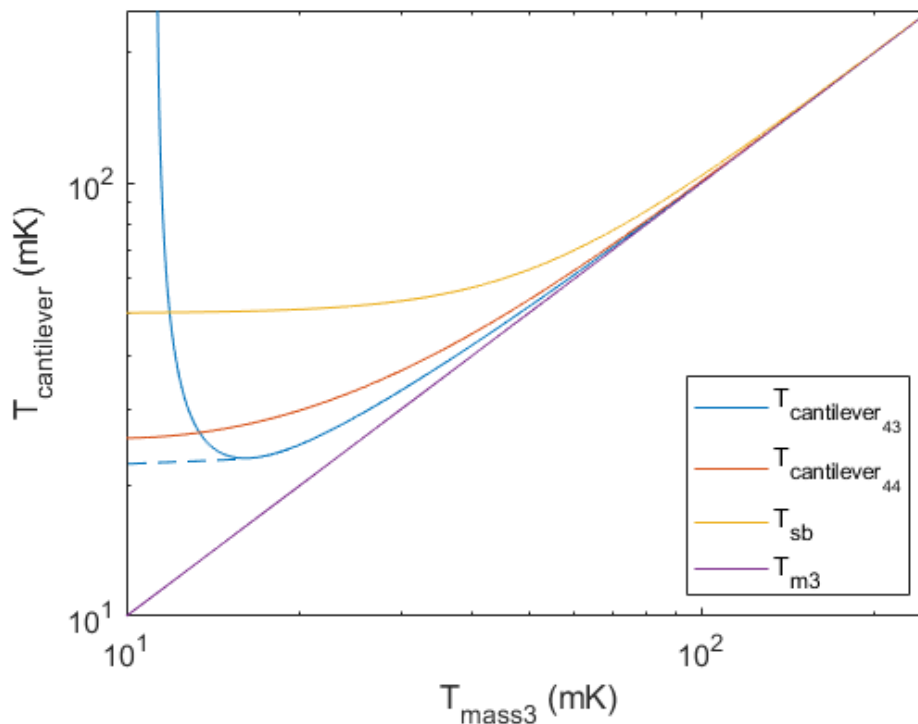


**Figure 4.19:** The model qualitatively describes the observed saturation behaviour for both runs. Using the measured damping of run 43 and 44, qualitative predictions can be done with respect to the saturation behaviour, which are plotted in blue and red.



## Outlook

### 5.0.1 Possible Improvement

Even though the results presented in this thesis offer significant advances over earlier work in the Oosterkamp group and those published to this day, there is still room for improvement. In this chapter we briefly reflect upon the possibilities that remain within our current setup and will expand upon possible ways to alter the setup in our favour.

### 5.0.2 Current Setup

The current setup clearly has shortcomings, as the extra coupling to the environment destroys the linearity of figure 3.9 for low temperatures. However, choosing the measurement parameters in a smart way, the results can still be improved. First, as described in this section, the cantilevers position is crucial for the observed amount of saturation. No systematic way has been found to find a position with minimal external coupling, but in future measurements it is advised to do a quick (30 min per data point) low temperature (15 – 40mK) sweep to chart the saturation behaviour of that position. Move the cantilever until a very steep saturation is seen with low temperature offset. Then, do a long temperature sweep in the range 40 – 100mK with as many different temperature data points as possible (30 or so). This high number of data points will convince us that the we are in the linear regime and it will greatly reduce the standard deviation on the offset of the linear fit. The latter will make a great difference in maximum measured force noise (95%) as this has been limiting so far, as was seen in the table in section ??.

This practical view on doing measurements is fine for more detailed

results in the short term, but in the long term it is imperative to gain an understanding of what component in the setup acts as the second heat bath. We offer two remarkable observations here that can hopefully guide future researchers in the right direction. First, a huge shift in resonance frequency was observed due to changes in the sample holder temperature, as can be seen in figure 6.4. Before these experiments were done, the shifting of resonance frequency was attributed to changes in the cantilever stiffness when it was cooled down. However it was found that the mass 3 temperature has no influence on the resonance frequency. We hypothesize that the same coupling mechanism that works as a dissipation channel for the cantilever energy also alters the resonance frequency. As the cantilever's mass is unchanged, this mechanism increases the spring constant of the cantilever at low environment temperature. When comparing the

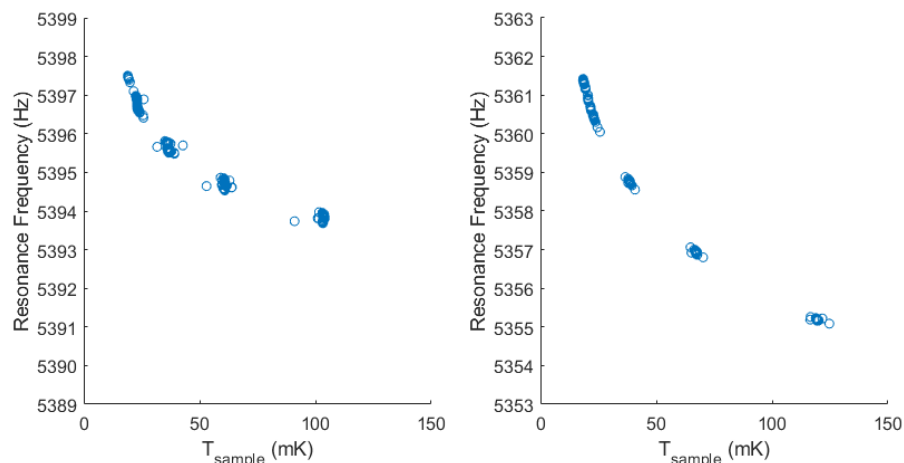


**Figure 5.1: The magnitude of the resonance frequency shift varies for different runs, but is always inversely dependent on sample temperature.** a) The frequency shift in run 43 was smaller in magnitude and occurred at lower temperatures (scatter of all data from figure 4.14). b) Data from run 44 (2019-02-22/23).

shifting of the resonance frequency in different runs, a peculiar fact is observed. The shift was stronger and appeared over a broader temperature range in run 44 with respect to run 43, shown in figure 5.1. This reminds us vaguely of the saturation behaviour of these runs, which was also stronger and over a broader temperature range in run 44. However, as the underlying mechanism for the shift is unclear we can only speculate that it is somehow related to the coupling  $\gamma_{sb}$ . Also, it remains unclear what drives the absolute cantilever frequency, apart from its temperature dependence. Second, throughout our experiments, we encountered diffi-

culty when trying to do an independent measurement of the cantilever's coupling to the SQUID. This can be done sending an input through the pick-up loop and measuring the transfer function. In these calibrations an unexplained phase shift was seen, possibly due to an unknown resistance in the detection circuitry. We advise future researchers to start by analyzing one of these two phenomena which we have not been able to explain.

### 5.0.3 Improved Setup

There are three directions that can be taken to improve the current setup. First, additional noise sources can be eliminated. When it is clear what exactly causes the saturation behaviour, one can remove this element or design a new setup wherein its influence will be minimal. This can for example be done by designing an own thermostat for the SQUID and fully isolating it from the pick-up loop, using high frequency filters.

Second, one can increase the detection sensitivity by using a cantilever with an even higher Q-factor. Of course, the damping from a coupling to a second heat bath should not be dominant in that case. A higher Q-factor decreases the thermal force noise acting on the cantilever (as this scales as  $T/Q$ ) and therefore magnifies the sensitivity for excess force noise. Note however that this will not improve the upper bounds if there are still other white noise sources acting on the setup, as these will also be amplified. It does give a better estimation on the magnitude of the noise that is acting on the setup.

Third, one can consider adding extra sources of CSL noise on the cantilever. In run 44, we have produced a cantilever with a tiny gold fragment on top which is expected to generate a high CSL force noise. Unfortunately, we did not manage to do any measurements on this cantilever, presumably because it was positioned too far from the pick-up loop. Designing systems like this with higher densities and big surface area will make it possible to exclude a bigger region in the CSL parameter space if a similar force noise is measured.

### 5.0.4 The Future of CSL

We are confident that by applying these alterations, future experiments will be able to lower the upper bounds of  $\lambda_{CSL}$  another order of magnitude in order to fully rule out Adler's proposal for  $r_c = 10^{-7}$  m. If however, multiple different experiments get stuck at the same upper bound,

the possibility exists that CSL can actually be proven true. This will be an extremely difficult challenge for the scientists involved as they can expect extensive criticism and inquisition of their experiments. The author of this thesis wishes them the best of luck in their quest to make quantum mechanics a bit less weird, if only a bit.

## **Acknowledgements**

This research was made possible by financial support from the Dutch Association for Scientific Research (NWO) and the Foundation for Fundamental Research of Matter (FOM). The author would like to thank the Oosterkamp group for their support, prof. dr. ir. T.H. Oosterkamp and dr. M. de wit in particular.

# Chapter 6

## Appendix

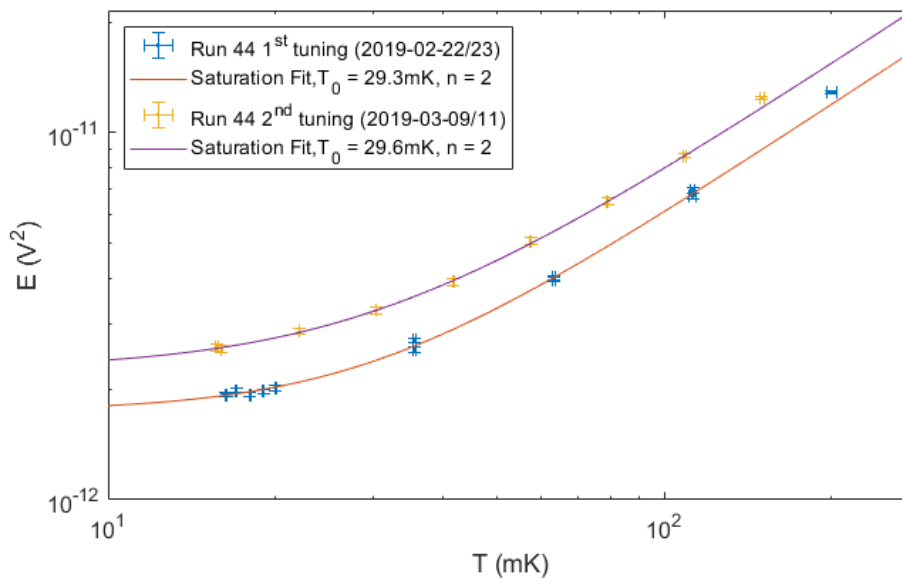


**Figure 6.1: SQUID tuning does not influence the saturation parameters.** It is thought that only the position of the cantilever determines the coupling to the environment and thus the saturation properties.

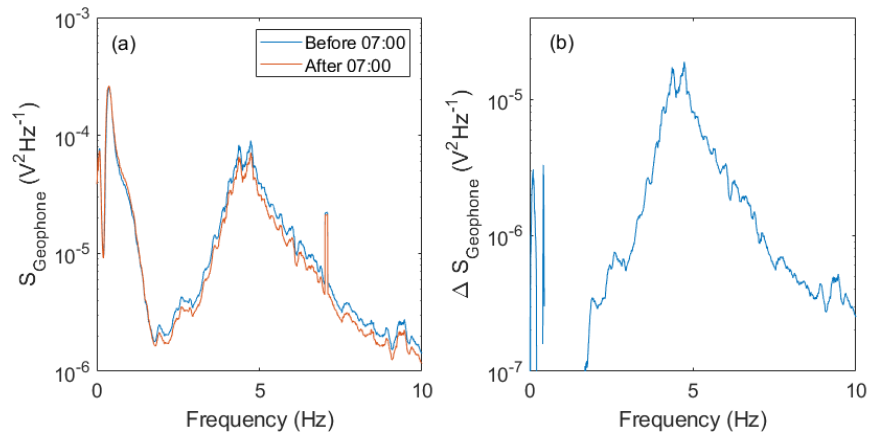


**Figure 6.2:** During mornings the squared amplitude at low frequencies of the geophone is increased. a) The vibration noise captured by the geophone is seen to increase over a range of low frequencies (1 – 10 Hz). b) Difference in noise between night and morning, examined with the data from figure 4.8.

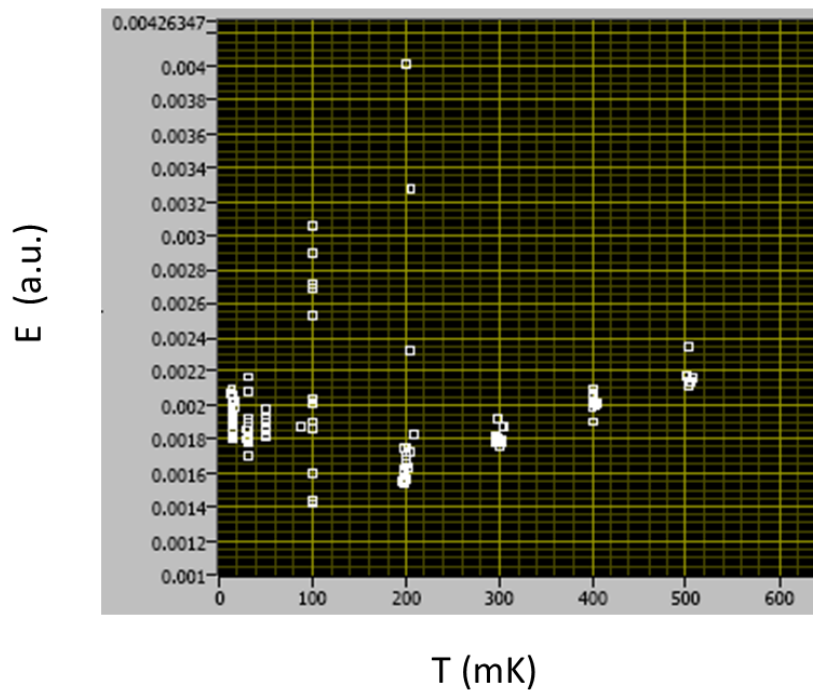


**Figure 6.3:** Apparent rise in cantilever temperature at lower bath temperatures. Data from Wagenaar (2015-02-15)

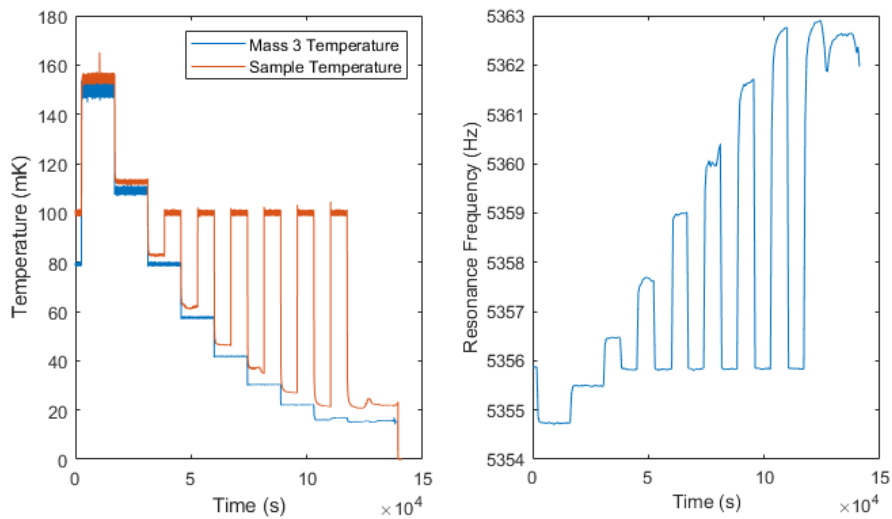


**Figure 6.4:** *The shifting of the resonance frequency is driven by the temperature of the sample. a) The temperature log from the measurement done on 2019-03-09/11 (Run 44) is shown. b) The resonance frequency was determined using a Lorentzian fit as described in section 3.3.2. Not the temperature of mass 3, which is the biggest driver of the cantilever temperature, but the sample temperature makes the resonance frequency increase at low temperatures.*



# Bibliography

- [1] M. Born, *A Suggestion for Unifying Quantum Theory and Relativity*, Proceedings of the Royal Society of London. Series A. Mathematical and Physical Sciences (2006).
- [2] B. Green, *The elegant universe: superstrings, hidden dimensions, and the quest for the ultimate theory*, Choice Reviews Online (2013).
- [3] A. Bassi, K. Lochan, S. Satin, T. P. Singh, and H. Ulbricht, *Models of wave-function collapse, underlying theories, and experimental tests*, Reviews of Modern Physics (2013).
- [4] L. Rosenfeld, *Early history of Quantum mechanics*, Nature **166**, 883 (1950).
- [5] J. J. Sakurai and R. L. Liboff, *Modern Quantum Mechanics*, American Journal of Physics (2005).
- [6] D. Griffiths, *Introduction to Quantum Mechanics*, 2005.
- [7] G. C. Ghirardi, A. Rimini, and T. Weber, *Unified dynamics for microscopic and macroscopic systems*, Physical Review D (1986).
- [8] G. C. Ghirardi, P. Pearle, and A. Rimini, *Markov processes in Hilbert space and continuous spontaneous localization of systems of identical particles*, Physical Review A (1990).
- [9] A. Vinante, M. Bahrami, A. Bassi, O. Usenko, G. Wijts, and T. H. Oosterkamp, *Upper Bounds on Spontaneous Wave-Function Collapse Models Using Millikelvin-Cooled Nanocantilevers*, Physical Review Letters (2016).

- 
- [10] A. Vinante, R. Mezzena, P. Falferi, M. Carlesso, and A. Bassi, *Improved Noninterferometric Test of Collapse Models Using Ultracold Cantilevers*, *Physical Review Letters* (2017).
- [11] J. von Neumann, *Mathematical Foundations of Quantum Mechanics*, 1955.
- [12] S. L. Adler, *Lower and upper bounds on CSL parameters from latent image formation and IGM heating*, *Journal of Physics A: Mathematical and Theoretical* (2007).
- [13] G. Fowles and G. Cassiday, *Analytical Mechanics*, 2005.
- [14] M. de Voogd, *MRFM and the Spin Bath*, 2018.
- [15] P. R. Saulson, *Thermal noise in mechanical experiments*, *Physical Review D* (1990).
- [16] O. Usenko, A. Vinante, G. Wijts, and T. H. Oosterkamp, *A superconducting quantum interference device based read-out of a subattoneutron force sensor operating at millikelvin temperatures*, *Applied Physics Letters* (2011).
- [17] M. De Wit, *Advances in SQUID-detected Magnetic Resonance Force Microscopy*, Dissertation Leiden University , 11 (2019).
- [18] M. H eritier, A. Eichler, Y. Pan, U. Grob, I. Shorubalko, M. D. Krass, Y. Tao, and C. L. Degen, *Nanoladder Cantilevers Made from Diamond and Silicon*, *Nano Letters* (2018).
- [19] M. De Wit, G. Welker, K. Heeck, F. M. Buters, H. J. Eerkens, G. Koning, H. Van der Meer, D. Bouwmeester, and T. H. Oosterkamp, *Vibration isolation with high thermal conductance for a cryogen-free dilution refrigerator*, *Review of Scientific Instruments* (2019).
- [20] J. J. Wagenaar, A. M. Den Haan, J. M. De Voogd, L. Bossoni, T. A. De Jong, M. De Wit, K. M. Bastiaans, D. J. Thoen, A. Endo, T. M. Klapwijk, J. Zaanen, and T. H. Oosterkamp, *Probing the Nuclear Spin-Lattice Relaxation Time at the Nanoscale*, *Physical Review Applied* **6**, 1 (2016).
- [21] M. De Wit, G. Welker, J. M. De Voogd, and T. H. Oosterkamp, *Density and T1 of Surface and Bulk Spins in Diamond in High Magnetic Field Gradients*, *Physical Review Applied* (2018).